# Fast Prediction of Ionic Epitaxial Interfaces with Ogre Demonstrated for Colloidal Heterostructures of Lead Halide Perovskites

*Stefano Toso[1,†], Derek Dardzinski[2,†], Liberato Manna[1]*, Noa Marom,[2,3,4]**

[1]Nanochemistry Department, Istituto Italiano di Tecnologia, Genova, 16163, Italy

[2]Department of Materials Science and Engineering, Carnegie Mellon University, Pittsburgh, PA, 15213, United States

[3]Department of Physics, Carnegie Mellon University, Pittsburgh, PA, 15213, United States

[4]Department of Chemistry, Carnegie Mellon University, Pittsburgh, PA, 15213, United States

[†]These authors contributed equally

E-mail: liberato.manna@iit.it, nmarom@andrew.cmu.edu

Keywords: epitaxy, interface, heterostructure, perovskite, structure prediction, DFT

## Abstract

Colloidal epitaxial heterostructures are nanoparticles composed of two different materials connected at an interface, which can exhibit properties different from those of their individual components. The ability to combine dissimilar materials offers wide opportunities to create functional heterostructures. However, the design stage often focuses on combining materials based on the desired properties, while structural compatibility at the interface is overlooked. To accelerate the design of new heterostructures between ionic materials, which encompass most colloidal semiconductors, we implemented a new workflow in the Ogre code for the prediction of epitaxial interfaces. Thanks to a pre-screening of candidate models based on charge balance and an electrostatic force-field for fast energy evaluations, our workflow can optimize complex interfaces in just a few minutes on a simple laptop. We validate our approach for heterostructures involving lead halide perovskites, for which Ogre produces interface models in excellent agreement with the experiments. Further case studies demonstrate how Ogre can be used to (re-)interpret experimental data and propose atomistic models for previously unknown interfaces involving ionic materials, such as metal halides and oxides. The Ogre package is available on GitHub, and users without computational expertise can run it via the *OgreInterface* desktop application, available for Windows, Linux, and Mac.

## 1. Introduction

Colloidal heterostructures are nanoparticles composed of two materials connected at an interface. Such architectures can profitably combine the properties of their components, and may exhibit unique functionalities emerging from their interaction. Prominent examples are core-shell quantum dots[1–3] and photocatalytic nanocomposites,[4–7] whose properties stem directly from the electronic structure of the junction. The increasing availability of colloidal materials has encouraged a property-driven approach to the design of new heterostructures, where materials are paired based on desired features like band alignment, plasmon resonance, or other functionalities.[8–12] However, materials selected based on their properties are not always structurally compatible,[13] and the absence of suitable structural relations may lead to the formation of amorphous or highly defective interfaces. Such heterostructures might still be useful if the target functionality is insensitive to the nature of the interface, as is the case for protective oxide shells.[14,15] However, heterostructures expressing electronic, magnetic, and optical properties that arise from quantum interactions at the junction may be impaired.[16–25]

To express their full potential, such heterostructures require epitaxial interfaces that ensure a precise matching between the two materials, and can grow virtually defect-free. Indeed, the most successful colloidal heterostructures are fully epitaxial architectures between isostructural materials (e.g., CdSe/CdS, CdSe/ZnSe, InP/ZnS),[2,26–29] which combine outstanding optoelectronic properties with a simple and predictable growth process. However, isostructural interfaces cover only a small fraction of the wide design space offered by colloidal chemistry, and the increasing number of reported heterostructures between non-isostructural materials, often obtained by chance, suggests that there is much more to explore.[30,31,40–42,32–39]

Nevertheless, synthesizing new heterostructures is a painstaking process of trial and error, as even compatible materials often tend to crystallize separately, and the co-presence of many elements in the reaction medium can lead to competing byproducts. Hence, failing to couple a specific pair of materials raises the question of whether such a heterostructure is intrinsically impossible to grow, or if the right conditions have not been found yet. Moreover, the morphology of nanocrystals may evolve during post-synthetic treatments, complicating the identification of facets involved in the interface growth.[43–48] Finally, the instability of some colloidal nanomaterials under an electron beam can hinder the collection of atomic resolution images, which are needed to verify if a heterostructure is truly epitaxial and determine the interface structure.[49,50]

These challenges can be addressed through computer simulations, which help direct synthetic efforts toward materials that are likely to match epitaxially, and can provide models to assist the interpretation of experiments. Several tools for the prediction of interface structures have been developed to this end.[47,51–58] These often employ hierarchical workflows, in which fast methods like classical force fields, score functions, or machine learning are used for the initial screening of models, followed by density functional theory (DFT) calculations to predict the structure and properties of the most promising candidates.[57–64] A similar approach is implemented in the Ogre open-source Python package for the prediction of organic and inorganic epitaxial interfaces.[65–68] However, the tools currently available are not well-suited to identify prospective interfaces that could be grown by colloidal chemistry, as this requires a quick evaluation of numerous interfaces rather than the detailed simulation of a few. The task is further complicated by the complex compositions and structures adopted by many colloidal materials, like the lead halide perovskites studied here, which make approaches that rely heavily on DFT less suitable. Lastly, most structure prediction codes are designed for specialists, while synthetic chemists would benefit from tools that are easy to use, and do not require coding experience or access to advanced computing facilities.

To address these needs, we have implemented in Ogre a fast workflow for the prediction of epitaxial interfaces between polar compounds, which encompass most colloidal nanomaterials (e.g. $CsPbBr_3$, CdS, ZnO, etc.). This includes two new features that take advantage of the predominantly ionic nature of these materials to dramatically accelerate predictions. The first is a preliminary screening of interface models based on charge balance, which reduces the computational load by eliminating unreasonable candidates. The second feature is a classical potential consisting of a Coulomb term[69,70] and a repulsive Born term,[65,71] whose parameters are determined automatically based on the bulk structures of the input materials. This potential allows to quickly evaluate the energy of candidate structures, and can produce interface models and energy rankings in good agreement with DFT at a fraction of its computational cost. These strategies enable predicting the structure of epitaxial interfaces between polar materials in just few minutes on a simple laptop, making Ogre an excellent screening tool. We note that this approach is not suitable when the dominant interactions are not electrostatic, as is the case for metallic, covalent, and van der Waals dispersion bonding. To cover these cases, DFT, machine-learned potentials, and alternative score functions are available in Ogre.[65–68]

In what follows, the new Ogre workflow for the prediction of polar epitaxial interfaces is presented and validated extensively for several case studies. In **Section 2.1**, we illustrate the full workflow in detail, using the $CsPbBr_3/Pb_4S_3Br_2$ colloidal heterostructures reported by some of us as an example.[72,73] For this system, Ogre correctly identifies all the known epitaxial relations, and for the case study of the (100)∥(010) orientation, it produces an interface model that matches both DFT-based predictions and high-resolution scanning transmission electron microscopy (HR-STEM) images of the heterostructures. In **Section 2.2**, we demonstrate how Ogre can help elucidate the outcome of a synthesis by revisiting a previous study of perovskite/lead sulfochloride heterostructures, conducted by some of us.[74] Specifically, the empirical observation that $CsPbCl_3$ nanocrystals template the selective nucleation of $Pb_4S_3Cl_2$ while suppressing the growth of the competing phase $Pb_3S_2Cl_2$, is rationalized based on Ogre's predictions of lattice matching and interface stability. In **Section 2.3**, we revisit several heterostructures involving $CsPbBr_3$ to demonstrate how Ogre can help assign structural models to newly synthesized interfaces, taking advantage of characterization results as a part of the prediction workflow.[32,42,75,76] A prominent example is the $CsPbBr_3$/Pb-Bi-S heterostructures recently reported by some of us,[35] whose hitherto unknown composition and interface connectivity are unraveled by combining information from HR-TEM experiments with Ogre predictions. Finally, in **Section 2.4** we demonstrate Ogre's broad applicability beyond colloidal metal halides by reproducing the structure of known heteroepitaxial interfaces between pairs of oxides, which are among the most studied polar materials for thin film growth.[77–83]

In addition to being efficient and versatile, Ogre is accessible to non-specialized users via the *OgreInterface* desktop application, available for Windows, Linux, and Mac. All scripts and reference bulk structures needed to reproduce the results presented here are available as Supplementary Material, and serve as examples for newly approaching users. By being directly accessible to synthetic chemists, we expect Ogre to become a versatile and powerful tool for the discovery and investigation of new epitaxial heterostructures between polar materials.

## 2. Results and Discussion

### 2.1. Ogre workflow demonstrated for $CsPbBr_3/Pb_4S_3Br_2$

Given the crystal structure of two materials, *A* and *B*, Ogre first identifies all favorable commensurate epitaxial relations between them, and then attempts to predict the structure of the resulting interfaces. The output is a set of atomistic models with optimized epitaxial registry (i.e., lateral offset) and interface distance, ranked by energy from the most to the least stable. The prediction workflow proceeds through three steps, illustrated in **Figure 1**: *lattice matching*, *interface generation*, and *surface matching and ranking*. **Sections 2.1.1-2.1.3** demonstrate each step of the algorithm for the (100)∥(010) – $CsPbBr_3/Pb_4S_3Br_2$ epitaxial interface, which some of us have previously characterized in the form of colloidal heterostructures.[72] In **Section 2.1.4**, the performance of the Ogre classical potential is validated against DFT for the same interface. We note that in this work $CsPbBr_3$ is treated as cubic despite adopting a slightly distorted orthorhombic structure.[84–87] This approximation greatly simplifies the discussion of results, and does not adversely affect the outcome of predictions (see Figures S1-7 and Tables S1-4).

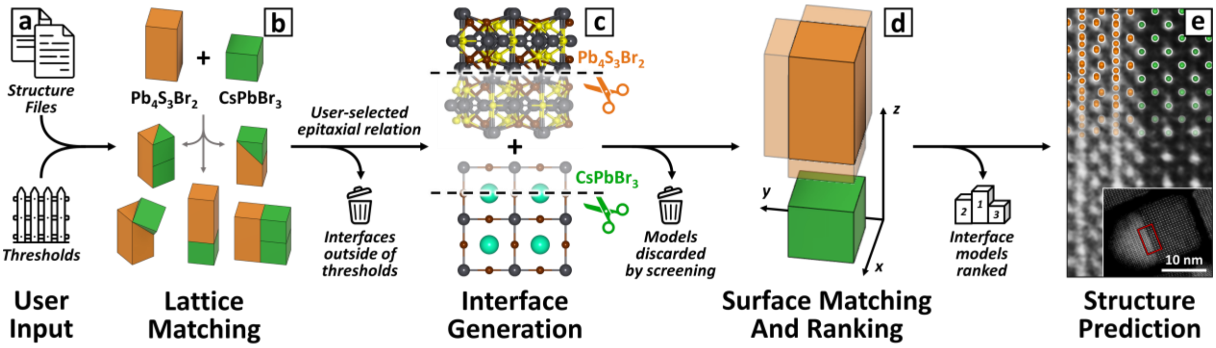

**Figure 1. Ogre interface prediction workflow.** a) Ogre takes as an input the bulk structures of two materials, along with user-defined thresholds for strain, supercell area, and the Miller indices of lattice planes to consider. b) The *lattice matching* step identifies all the commensurate supercells that yield domain-matched interfaces within the specified thresholds. c) For selected epitaxial orientations, the *interface generation* step creates all possible surface terminations for both materials, and combines them to construct atomistic models of the interface. d) For each model, the *surface matching and ranking* step identifies the optimal epitaxial registry (i.e., lateral offset) and distance between the two domains, using a fast electrostatic potential to evaluate energies. e) The output is a set of atomistic models ranked by stability. Top-ranked models can be compared with available experimental data, as demonstrated here for a $Pb_4S_3Br_2/CsPbBr_3$ heterostructure (only heavy atoms shown for clarity). HR-STEM images adapted with permission.[72] Copyright 2023, American Chemical Society.

### 2.1.1 Lattice matching

The *lattice matching* step uses the Zur-McGill algorithm[51] to identify commensurate epitaxial relations between the two materials, denoted here as $(hkl)_A /\!/ (h'k'l')_B$ based on the lattice planes being matched. In short, the algorithm attempts to combine multiple 2D-cells describing the lateral periodicity of $(hkl)_A$ and $(h'k'l')_B$ planes to construct a common 2D-supercell that can represent both materials at the interface. An epitaxial match is found if such supercell(s) exist within the user-defined constraints for strain and area. We note that one $(hkl)_A /\!/ (h'k'l')_B$ combination may produce several non-equivalent 2D-supercells that differ by a relative rotation of the two materials around an axis perpendicular to their contact plane.[65] In that case, the smallest 2D-supercell is selected (see Figure S8 and related discussion). To avoid any ambiguities, Table S5 specifies for all interfaces discussed in this work a pair of lattice vectors that are parallel to each other in the plane of the interface, denoted here as $[hkl]_{\mathrm{A}} \Uparrow [h'k'l']_{\mathrm{B}}$.

At this stage, the user can impose constraints on strain and supercell area to exclude implausible matches. In general, high strain is unfavorable, as it can lead to the formation of defects at the interface or even hinder its growth. However, a certain degree of mismatch is tolerable, depending on the type of interface being studied. For example, the strain limit for high-quality epitaxial semiconductor films is considered to be around 2%.[88] Conversely, nanoscale interfaces tend to be more tolerant because strain can be effectively absorbed by lattice deformations if the contact surface is limited to few nm$^2$. For instance, the $CsPbBr_3$/$CsPb_2Br_5$ heterostructures reported by Zheng et al. accommodate a 2.7% mismatch by bending into rings where the material with the largest lattice step faces outward (see **Section 2.2**).[32] Other examples of high-strain colloidal interfaces are CdS/CdSe (4.2%)[89] and the rather extreme InAs/ZnS (12.0%).[90] For the colloidal heterostructures studied here, we set the strain threshold to 10%.

For setting the area threshold there are conflicting considerations. On the one hand, larger supercells enable finding commensurate domains with lower strain, approaching the limit where an infinite area produces supercells without any strain. On the other hand, smaller supercells increase the chance of good atom-to-atom correspondence at the interface because the lattice sites of the two materials are more likely to coincide. By default, Ogre sets the surface area threshold, $S_T$, to:

$$S_T = 2 \times \max[S_A(hkl)\ ;\ S_B(h'k'l')] \tag{1}$$

In short, for each $(hkl)_A /\!/ (h'k'l')_B$ pair, $S_T$ is set to twice the area of the largest 2D-cell among the two planes. This enables finding supercells that can encompass up to two single-material cells positioned side-by-side, thus allowing for a more extended interface repeating unit. The user can select a numerical hard threshold if needed (see Equation S7 and related discussion).

The user may also impose constraints on the Miller indices to be searched, based on their pre-existing knowledge of the system of interest. For example, the planes exposed by one or both materials might be known, as is the case for well-faceted nanocrystal seeds, or for the epitaxial growth of a thin film on a single-crystalline substrate. In the absence of such information, or if multiple hypothetical orientations are being considered, it is still reasonable to limit the search to low Miller indices because high-index crystal terminations are usually less stable, and therefore rarely exposed.[43–46,48,91]

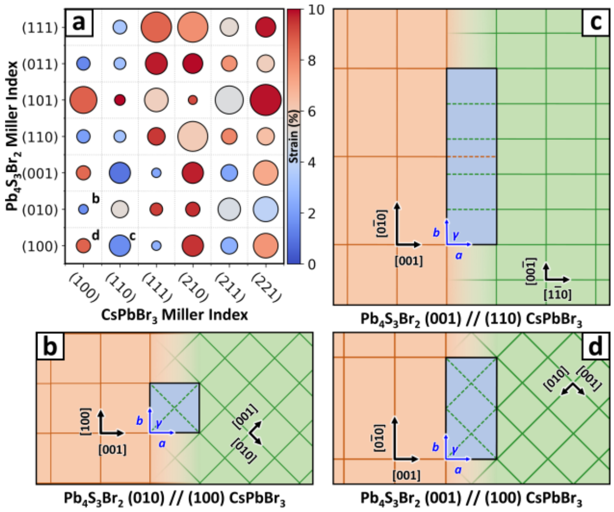

**Figure 2. *Lattice matching* results for $CsPbBr_3/Pb_4S_3Br_2$.** a) Domain-matched interfaces identified within the specified constraints. Each circle indicates a match, with the color corresponding to the strain and the size representing the interface area. The interfaces marked with letters have been reported experimentally, and their 2D-supercell is shown in the corresponding panels. b-d) Supercells of the $CsPbBr_3/Pb_4S_3Br_2$ interfaces reported in (b) Ref. 72 and (c,d) Ref. 92. The $CsPbBr_3$ 2D-lattice is colored in green, the $Pb_4S_3Br_2$ 2D-lattice in orange, and the domain-matched commensurate 2D-supercell is shown in blue.

**Figure 2** summarizes the lattice matching results for the $CsPbBr_3/Pb_4S_3Br_2$ system. For ease of visualization $h,k,l \leq 1$ for $Pb_4S_3Br_2$ and $h,k,l \leq 2$ for $CsPbBr_3$ are shown here (see Figure S9 for a more extended search). Each circle in **Figure 2a** corresponds to a domain-matched epitaxial relation identified within the constraints: the color indicates the strain, while the size represents the supercell area. Interfaces reported experimentally are marked with a letter, pointing to the corresponding 2D-supercell (**Figures 2b-d**).[72,92] The (100)⫽(010) – $CsPbBr_3/Pb_4S_3Br_2$ interface (**Figure 2b**) stands out for having both a low strain of 1.6% and a small area of 68 Å$^2$. Indeed, this interface was the first to be reported and fully characterized by some of us for the $CsPbBr_3/Pb_4S_3Br_2$ system.[72]

Ogre also identifies two additional epitaxial relations that were recently reported by Das et al:[92] the (110)⫽(001) interface, with 0.9% mismatch and an area of 241 Å$^2$ (**Figure 2c**), and the (100)⫽(001) interface, with 8.6% mismatch and an area of 136 Å$^2$ (**Figure 2d**). Because these interfaces were observed in nanoscale heterostructures, the contact surface between the two materials was likely small enough to tolerate what would otherwise be a high strain value. It is worth noting that the $a$ and $c$ lattice parameters of $Pb_4S_3Br_2$ are very close, leading to $(hkl) \approx (lkh)$ for this material. This causes similarities between the matches found by Ogre for the (100) and (001) planes of $Pb_4S_3Br_2$, and would also complicate the experimental distinction between these orientations. In the absence of atomic-resolution images of the interface, we cannot exclude that some of the heterostructures observed by Das et al.[92] might have adopted alternative epitaxial relations (see Figures S10-14 and Tables S6-10 for further discussion).

Based on the results shown in **Figure 2**, there are several additional plausible matches that have not been reported experimentally. For example, the (111)⫽(100) interface (2.5% strain and 118 Å$^2$ area) and the (110)⫽(110) interface (3.1% strain and 145 Å$^2$ area) appear comparable to the (100)⫽(010) interface reported by some of us, and more favorable than those reported by Das et al.[92] It is likely that these interfaces have not been observed owing to the known tendency of $CsPbBr_3$ nanocrystals to express the (100) facets.[43,93]

### 2.1.2. Interface generation

The *lattice matching* procedure relies solely on lattice parameters, with no consideration of interatomic interactions and bonding at the interface. To assess if any of the identified epitaxial relations can produce a chemically stable interface, an exhaustive set of atomistic models must be constructed and ranked by relative energy. To this end, Ogre cleaves the two materials at planes parallel to the interface to generate surface slabs with different terminations,[65,94] which are then combined to construct interface models. At this stage, Ogre can be set to distribute the strain on the two materials equally, as is the case in most colloidal heterostructures, or instead let the lattice of one material conform to the other, which might be better suited to describe the growth of a thin film on a bulk substrate.

**Figure 3** illustrates the construction of interface models for the (100)⫽(010) – $CsPbBr_3/Pb_4S_3Br_2$ interface.[72] Depending on the complexity of the materials involved, this process can result in a large number of candidate structures. Therefore, multiple strategies are implemented to minimize the number of models that proceed to the *surface matching and ranking* step of the algorithm, which is the most computationally intensive. Specifically, while generating slab models, Ogre clusters together nearly co-planar atoms to construct only chemically sound surface terminations. The resulting slabs are then screened to eliminate those that are equivalent by symmetry, thus avoiding redundancies (see Figures S15-16).

To further reduce the number of interface models, we have developed a fast screening algorithm based on the charge balance at the interface. To this end, each slab is assigned a surface charge $Q$, defined as:

$$Q = -\frac{\sum_i q_i \cdot d_i}{D} \qquad (2)$$

where $i$ runs over all ions in the slab, $q_i$ is the ion charge, $d_i$ is its distance from the interface, and $D$ is the total thickness of the slab (see Equations S8-S9 and Figure S17 for derivation). Conceptually, $Q$ represents the uncompensated charge found at the surface of each material, which will interact with the other material to construct the interface. Because charges of the same sign repel each other, interfaces formed by [+/+] or [–/–] slab pairs can be immediately excluded based on the sign of $Q$.

In principle, the magnitude of $Q$ could also be used to identify [+/–], [+/0], and [– /0] models that do not achieve full charge balance at the interface, which could serve as a further screening criterion. However, plenty of examples for unbalanced and yet stable interfaces have been reported, such as $Sm_2CuO_4/LaFeO_3$,[95] $LaAlO_3/SrTiO_3$,[96] and many Si/oxide[97] or metal/oxide[98] interfaces. This is possible because charge imbalance can be locally compensated by the formation of defects (ionic compensation) or a change of oxidation states (electronic compensation), which are often considered as the origin of 2D-conductivity in epitaxial interfaces between insulators.[96,99,100]

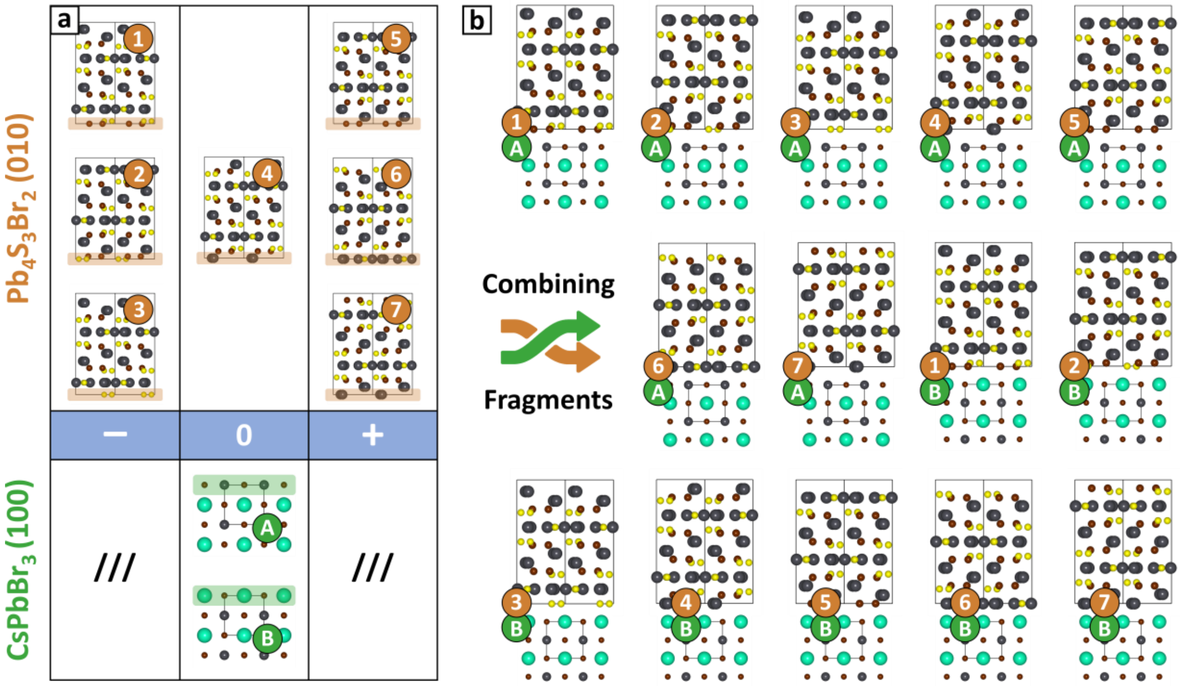

**Figure 3. Interface generation.** a) Possible terminations for the (010) $Pb_4S_3Br_2$ and (100) $CsPbBr_3$ surfaces. The +, 0, and – symbols refer to the surface charge of each slab. Colored shadings indicate the side of the slab that will contact the other material to form the interface, which is where the charge is calculated. b) Models of all the (100)⫽(010) – $CsPbBr_3/Pb_4S_3Br_2$ non-equivalent interfaces obtained by combining the slabs in panel (a), shown prior to the *surface matching* step. Cs atoms are colored in cyan, Pb in gray, S in yellow, and Br in brown.

The effectiveness of such compensation mechanisms depends on the materials involved, as not all elements can assume multiple oxidation states, and different structures might tolerate defects to a lesser extent than others. Furthermore, considering charge compensation mechanisms requires simulations that are too elaborate to be performed at a preliminary screening stage. For example, achieving a realistic concentration of defects may require large supercells, and multiple configurations must be considered to account for their random distribution. Conversely, variable oxidation states can be implicitly handled by DFT without affecting the size of the simulation, but pose challenges for classical force fields that explicitly assign a charge to atoms. Nevertheless, **Section 2.1.3** shows that the classical potential used for *surface matching and ranking* can handle unbalanced interfaces even in the absence of charge compensation mechanisms. Therefore, we opted to retain the [+/–], [+/0], and [– /0] cases for further scrutiny. The user can decide to exclude such interface models based on their knowledge of the system of interest.

Overall, the effectiveness of the preliminary screening strategies employed by Ogre depends on the materials under scrutiny. For example, **Figure 3** shows all the possible slab combinations considered further for the (100)∕∕(010) – $CsPbBr_3$/$Pb_4S_3Br_2$ interface. In this case, the number of $Pb_4S_3Br_2$ slabs is decreased from 14 to the 7 shown in **Figure 3a** by excluding symmetry-equivalent terminations, whereas the only two possible terminations for cubic $CsPbBr_3$ (i.e., CsBr and $PbBr_2$ planes formed by coplanar ions) cannot be reduced further. The advantage of clustering becomes more evident when considering the orthorhombic structure of $CsPbBr_3$, where ions are slightly shifted out of planarity. In that case, some of the possible cleavage planes would separate those ions, producing defective slabs with missing atoms at their surface. By clustering nearly co-planar ions together, Ogre identifies only the two chemically sound terminations also found for cubic $CsPbBr_3$ (see Figure S16). Moreover, as both $CsPbBr_3$ terminations yield slabs of the $Q = 0$ type, none of the 14 resulting interface models in **Figure 3b** are excluded based on charge balance. The $CsPbBr_3$/$Bi_2PbS_4$ interface discussed in **Section 2.3** provides an example of effective screening based on charge balance, where the number of models is reduced from 20 to 12 by excluding the [+/+] and [-/-] cases (see Figures S17-18).

### 2.1.3. Surface matching and ranking

When pairing two surface slabs, their relative position must be optimized to identify the best possible bonding configuration across the interface. To this end, Ogre employs particle swarm optimization[101,102] to efficiently explore the 3D space of parameters formed by the relative epitaxial registry (i.e., lateral *xy*-offset) and *z*-distance between the two slabs. The optimal configuration is the one that minimizes the energy of the interface model, $E_{AB}$. To visualize the outcome of *surface matching*, Ogre produces a 2D energy map by shifting one material on top of the other within the interface supercell at their optimal *z*-distance (**Figure 4a**), and computes an energy *vs* interfacial distance curve at their optimal *xy*-offset (**Figure 4b**). For visualization purposes, these plots display the adhesion energy $E_{adh}$, which is obtained by subtracting from $E_{AB}$ the energies of the two isolated slabs ($E_A$ and $E_B$). The sign of $E_{adh}$ indicates whether or not the resulting interface model is more stable than the two constituent surface slabs. In these maps, the global minimum of $E_{adh}$ corresponds to the relative slabs position that produces the most stable configuration, while local minima identify metastable configurations. As a part of its output, Ogre produces an atomistic model of the optimal interface configuration (**Figure 4c**), which can be opened with structure visualization programs like Vesta.[103]

Next, all surface-matched interface models are compared to identify the most stable interface structure. As a ranking metric, Ogre adopts the interface energy $E_{int}$, defined as:[67]

$$E_{int} = \frac{E_{AB} - (E_{AA'} + E_{BB'})/2}{S} \tag{3}$$

where $E_{AA'}$ and $E_{BB'}$ are the cleavage energies of the two materials $A$ and $B$ (i.e., the energy obtained when two slabs are re-assembled into a bulk-like slab with twice the thickness at a given cleavage plane), and $S$ is the supercell area. Essentially, $E_{int}$ compares the energy of the interface against that of the parent bulk materials, indicating how favorable it is to interrupt the growth of one domain and switch to the other (See Figures S19-22 for further discussion).

As mentioned above, evaluating the energy terms ($E_{AB}$, $E_{AA'}$, etc.) is the most computationally intensive task of the algorithm. To make this step computationally efficient, we have developed a classical potential that enables estimating the energy of interfaces at a fraction of the computational cost of DFT. In short, all energy terms are calculated using pair-wise interatomic potentials, consisting of an electrostatic Coulomb term computed via the damped-shifted force potential,[69,70,104] and a Born term accounting for short-range interatomic repulsions (see Equations S10-S16).[65,71] A cutoff of 18 Å is adopted because longer-range dispersion interactions are typically negligible in ionic materials. To enable our classical potential to describe a wide variety of polar materials, each pair-wise term is optimized for the corresponding pair of ions by fitting one free parameter in the Born term. This is performed by imposing that the energy minimum coincides with the equilibrium bond length found in the input bulk structures (see Equation S13). For bonds that only exist at the interface (e.g., $Cs^+$ – $S^{2-}$ in $CsPbBr_3/Pb_4S_3Br_2$), the optimal equilibrium distance is estimated based on the sum of ionic radii extracted from the two parent materials (see Figure S23). Because the fitting procedure relies on the input bulk structures as a reference, we find that the predicted interfacial distances are slightly more accurate when bonds that form between slabs also exist in the bulk materials. However, stable models typically converge to reasonable distances in either case.

We note that there are occasional instances of "non-bonding" interfaces, for which the energy *vs* interfacial distance curve is purely repulsive, and no minimum is found within the range considered (see Figure S22). This likely happens because our classical potential does not contain a long-range dispersion term. Because this only occurs when the electrostatic interactions between the two materials are not particularly favorable and the repulsive Born term dominates, we regard such interface configurations as not viable and discard them.

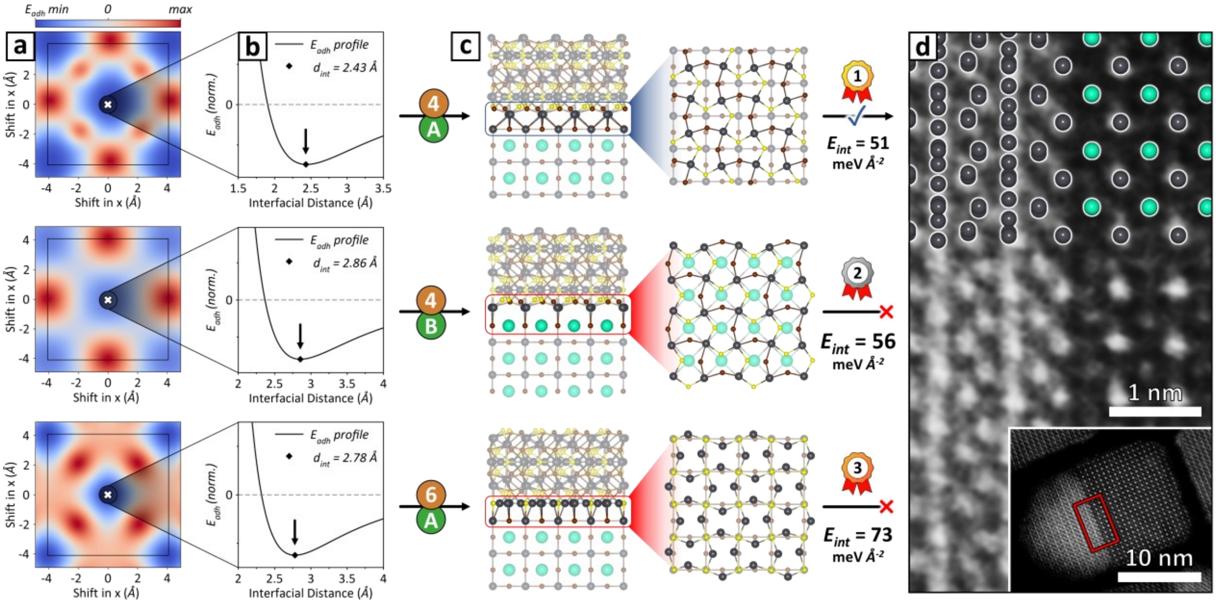

**Figure 4. Surface matching and ranking.** Results are displayed for the 4A, 4B, and 6A models of the (100)⫽(010) – $CsPbBr_3/Pb_4S_3Br_2$ interface, labeled as shown in **Figure 3**. a) Maps of $E_{adh}$ vs *xy*-offset with the optimal epitaxial registry marked by a cross. b) $E_{adh}$ *vs* interfacial distance curves, with the optimal *z*-distance indicated by an arrow. c) Interface models after the *surface matching* step. The side views (left) highlight the formation of bonds between slabs. The top-down views (right) of the interface planes show the atom-to-atom correspondence of anions and cations. The interface energies of the three models are also shown. d) HR-STEM image of a (100)⫽(010) – $CsPbBr_3/Pb_4S_3Br_2$ heterostructure, with superimposed the most stable model predicted by Ogre (see also Figure S4). Only heavy atoms are shown to ease the comparison with electron scattering contrast. Inset: lower magnification view of the same heterostructure. Microscopy data adapted with permission.[72] Copyright 2023, American Chemical Society. Cs atoms are colored in cyan, Pb in gray, S in yellow, and Br in brown.

---

Due to its purely electrostatic nature, our potential is restricted to compounds in which atoms carry a formal charge. This encompasses the majority of materials found in heterostructures synthesized colloidally with the notable exception of metal domains, that are relevant for plasmonic and catalytic applications.[7,9] However, metals often grow independently of epitaxial constraints due to their high tolerance for defects, to the point that non-substrate-specific growth strategies are available for technologically relevant elements (e.g., Au, Ag).[105,106] Likewise, our potential is not applicable to covalent and van der Waals materials, where non-electrostatic interactions are predominant. We remark that Ogre can predict the structure of interfaces involving non-polar materials by using other methods for surface matching and ranking, including geometric score functions, machine-learned potentials, and DFT, albeit the latter has a significantly higher computational cost.[65–68]

**Figure 4** shows the *surface matching and ranking* results for the three (100)⫽(010) – $CsPbBr_3/Pb_4S_3Br_2$ interface models ranked as most stable by our classical potential: **Panels 4a-b** illustrate the search for the optimal epitaxial registry and interface distance, while **Panel 4c** shows the resulting structures (see Figures S3-4 and Table S2 for a full account of the results). In each case, the procedure identifies the optimal bonding configuration, with the two slabs positioned so as to maximize attractive interactions and found within plausible distances. Notably, the two most stable interfaces, labelled 4A and 4B as in **Figure 3**, are of the [0/0] type and are very close in energy (52 vs 57 meV $Å^{-2}$). In contrast, the 6A model corresponds to a charge-unbalanced [+2/0] interface, and is significantly less stable (75 meV $Å^{-2}$). This suggests that a charge accumulation can destabilize the interface despite the good geometric matching between slabs and the presence of favorable $Pb^{2+}$–$S^{2-}$ electrostatic interactions, that are absent in the charge-balanced models 4A and 4B. We note, however, that the classical potential is unable to redistribute charges at the interface, as discussed in **Section 2.1.4**.

As shown in **Figure 4d**, the top-ranked model 4A matches well with experimental observations of the interface.[72] The model produced by Ogre was scaled to match the atomic-resolution image of the heterostructure without any adjustment to the relative position of the two domains, which attests to the accuracy of our prediction (see Figure S4 for a comparison with other models). To provide a practical estimate of the code's performance, the whole workflow illustrated in **Section 2.1** was executed on a mid-tier laptop in about ~100 s.

### 2.1.4. Validation against DFT

To further validate the performance of our classical potential, we compared the *surface matching and ranking* results for the (100)⫽(010) – $CsPbBr_3/Pb_4S_3Br_2$ interface to DFT. Because the choice of exchange correlation functional can significantly affect the outcome of DFT simulations, it is important to select one that adequately describes the materials of interest. Here, we have chosen the strongly constrained and appropriately normed (SCAN) functional[107] combined with the revised Vydrov and van Voorhis nonlocal correlation method (rVV10)[108,109] because it has been reported to reliably describe the dynamic tilting of octahedra and the phase transitions in halide perovskites.[110,111] In order to compare the results of the Ogre classical potential to DFT on an equal basis, the same workflow of *surface matching and ranking* was executed using DFT, with no structural relaxation beyond optimizing the relative position of the two rigid slabs.

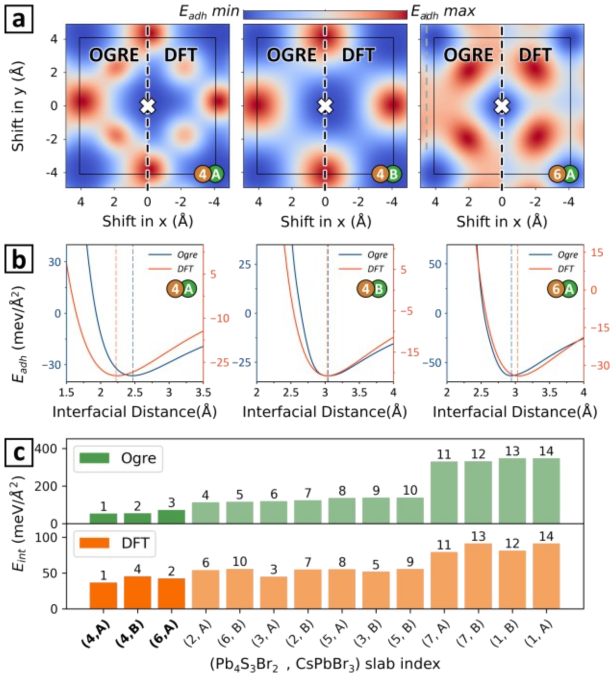

**Figure 5. Validation of *surface matching and ranking* by the Ogre potential against DFT.** a) $E_{adh}$ maps generated with the Ogre classical potential (left) and DFT (right) for the 4A, 4B, and 6A models of the (100)⫽(010) – $CsPbBr_3$/$Pb_4S_3Br_2$ interface (labeled as in **Figure 4**). Both methods identify the same epitaxial registry, marked by a cross. b) $E_{adh}$ *vs* interfacial distance curves for the same interfaces. c) Interface models ranked by computing $E_{int}$ with the Ogre electrostatic potential (top) and with DFT (bottom) with the 4A, 4B, and 6A models highlighted.

For the 4A, 4B, and 6A interface models shown in **Figure 4**, we compared the 2D energy maps (**Figure 5a**) and the $E_{adh}$ *vs* interfacial distance curves (**Figure 5b**) produced by the Ogre classical potential and by DFT. In all cases, our classical potential is in good agreement with DFT regarding the positions of the energy maxima and minima, meaning that the optimal in-plane epitaxial registry is correctly identified. The interfacial distance is in closer agreement with DFT for configurations 4B and 6A than for 4A, but it is consistently within 0.3 Å from the DFT results. Overall, our potential tends to overestimate the interfacial distances compared to DFT, with increasing inaccuracy as the interface models become less stable. This is likely because the classical potential does not include non-ionic contributions to the binding energy, and does not allow for charge density redistribution (see Table S11 for further discussion).

**Figure 5c** compares the ranking of interface models based on the Ogre classical potential and DFT. Both methods rank the experimental interface 4A as the most stable, and highlight a clear distinction between two groups of interfaces with lower and higher interface energies, separated by the gray dashed line. Within each group the interface energies are similar, leading to some reshuffling in the two rankings. Notably, the high-energy group is formed by models with strong charge imbalance at the interface (7A = 7B = [+4,0]; 1A = 1B = [-4,0]). Conversely, in the lower-energy group the Ogre classical potential favors the two charge-balanced interfaces 4A and 4B, whereas DFT ranks two charge-imbalanced interfaces as second and third (6A = [+2,0] and 3A = [-2/0], respectively). As mentioned above, both the 6A and 3A models feature favorable $Pb^{2+}$–$S^{2-}$ electrostatic interactions. It is possible that with DFT these interfaces are stabilized by charge density redistribution. We also note that local geometry relaxation at the interface may further change the stability ranking. In this respect, the Ogre potential can be used to quickly generate reasonable starting models for DFT-based relaxations.

## 2.2. Using Ogre to support synthetic efforts

In what follows, we demonstrate potential applications of Ogre in the field of colloidal nanomaterials, starting with the interpretation and prediction of possible outcomes for the synthesis of epitaxial heterostructures. Because synthesizing new materials is beyond the scope of this work, we use the results for lead sulfochlorides, reported by some of us, as a case study.[74]

Under typical colloidal synthesis conditions, the Pb-S-Cl system can lead to the growth of two competing materials: the pseudocubic $Pb_3S_2Cl_2$ (a phase with no equivalent for other halogens) and the orthorhombic $Pb_4S_3Cl_2$, which is structurally equivalent to the $Pb_4S_3Br_2$ sulfobromide discussed in **Section 2.1**.[73,74] Indeed, the presence of $CsPbCl_3$ nanocrystals in the reaction medium leads to the growth of $CsPbCl_3$/$Pb_4S_3Cl_2$ heterostructures similar to those in **Figure 4d**. Crucially, their formation coincides with a complete suppression of the pseudocubic competitor $Pb_3S_2Cl_2$. This outcome has been attributed to the growth of $Pb_4S_3Cl_2$ outpacing $Pb_3S_2Cl_2$ thanks to the epitaxial templating action of $CsPbCl_3$ seeds, which enables heterogeneous nucleation.[74] Such an interpretation relies on the assumption that no competing interface can form between the pseudocubic $Pb_3S_2Cl_2$ and $CsPbCl_3$, which we here confirm with Ogre. We note that the concept of promoting the growth of metastable phases by epitaxial templating is widespread in thin film growth,[112–115] but nascent in colloidal synthesis.

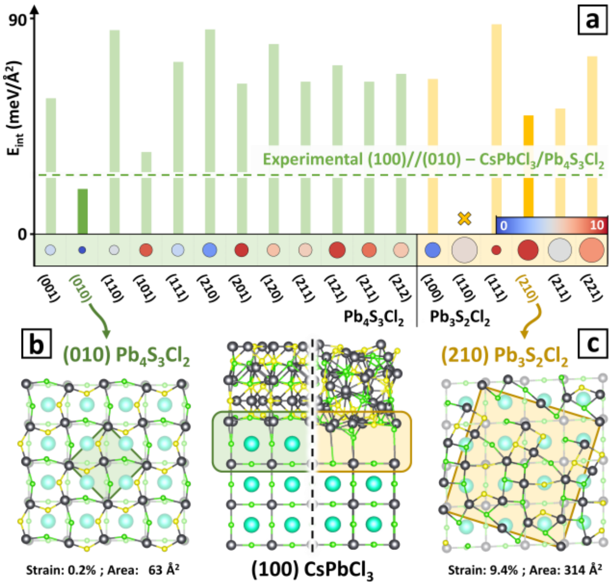

**Figure 6. Stability of $Pb_4S_3Cl_2$ *vs* $Pb_3S_2Cl_2$ on the (100) surface of $CsPbCl_3$.** a) *Lattice matching* and interface ranking results for the growth of $Pb_4S_3Cl_2$ (green) and $Pb_3S_2Cl_2$ (yellow) on the (100) surface of $CsPbCl_3$. The circle size corresponds to the interface area and the color corresponds to the strain. The green dashed line marks the $E_{int}$ value of the experimental interface, which is the 2nd-best model for the (100)∕∕(010) – $CsPbCl_3/Pb_4S_3Cl_2$ interface. Non-equivalent epitaxial relations leading to identical *lattice matching* results, like $(h,k,l) = (\bar{h},\bar{k},\bar{l})$ for $Pb_3S_2Cl_2$, have been aggregated for visualization purposes, and only the lowest $E_{int}$ value is shown. All models for the (100)∕∕(110) – $CsPbCl_3/Pb_3S_2Cl_2$ interface, marked with an ×, are found to be non-bonding. b) Model of the most stable interface formed between the (100) surface of $CsPbCl_3$ and $Pb_4S_3Cl_2$ (left: interface plane, center: side view). c) Model of the most stable interface formed between the (100) surface of $CsPbCl_3$ and $Pb_3S_2Cl_2$ (center: side view, right: interface plane). The corresponding 2D-supercells are also shown. Cs atoms are colored in cyan, Pb in gray, S in yellow, and Cl in green.

For $Pb_4S_3Cl_2$ no bulk crystal structure was available, and the nanocrystals obtained in Ref. 74 were too small to allow for a proper refinement by X-ray diffraction. Therefore, we extracted the lattice parameters directly from the HR-STEM images of a $CsPbCl_3/Pb_4S_3Cl_2$ heterostructure, via Fourier analysis of the lattice periodicity. To ensure maximum accuracy, we calibrated the image using the lattice constant of $CsPbCl_3$ (5.605 Å) as a reference. This resulted in a pseudo-tetragonal unit cell for $Pb_4S_3Cl_2$, with estimated lattice parameters $a = c =$ 7.94 Å and $b = 14.94$ Å. The atom positions inside the unit cell were determined starting from the analogous structure of $Pb_4S_3Br_2$ by performing DFT relaxation, using the SCAN+rVV10 functional with the lattice parameters fixed at the estimated values (see Figure S24). Because the $CsPbCl_3$ nanocubes acting as seeds expose the (100) facets, we focused on interfaces of the (100)∕∕(*hkl*) type with $h,k,l \leq 2$ for both $Pb_4S_3Cl_2$ and $Pb_3S_2Cl_2$ (see Figure S25).

**Figure 6** shows a comparison of Ogre's results for interfaces of $CsPbCl_3$(100) with $Pb_4S_3Cl_2$ and $Pb_3S_2Cl_2$ (see Table S12 for additional information). In the *lattice matching* step, all orientations considered for both $Pb_4S_3Cl_2$ and $Pb_3S_2Cl_2$ resulted in supercells within the specified thresholds for strain and area. Of these, the experimentally observed (100)∕∕(010) – $CsPbCl_3/Pb_4S_3Cl_2$ epitaxial relation already stands out as the most promising because of its lowest strain of 0.2% and smallest area of 63 $Å^2$. The results of *surface matching and ranking* confirmed that the (100)∕∕(010) – $CsPbCl_3/Pb_4S_3Cl_2$ orientation is indeed the most stable. The interface structure shown in **Figure 6b** is well-connected, which correlates with its high stability. We note that the lowest $E_{int}$ of 19 meV $Å^{-2}$ is obtained for the CsCl termination of $CsPbCl_3$, rather than the $PbCl_2$ termination observed in experiments. However, the $PbCl_2$-terminated model ranks as the second best for the (100)∕∕(010) – $CsPbCl_3/Pb_4S_3Cl_2$ interface, with an $E_{int}$ of 27 meV $Å^{-2}$ well below that of all the other interface models (dashed line in **Figure 6a**). This discrepancy in the surface termination is likely due to the tendency of perovskite nanocrystals to express a lead-rich surface,[116–118] which would provide a kinetic advantage to the growth of $PbCl_2$-terminated interfaces. However, other kinetic effects stemming from interactions with the reaction medium, that are not considered in our simulations, might play a role as well.

The most stable interface found for the competing $Pb_3S_2Cl_2$ phase is the (100)∕∕(210), with $E_{int} = 50$ meV $Å^{-2}$. A visual inspection of the interface connectivity, shown in **Figure 6c**, reveals the presence of several dangling bonds and undercoordinated ions, which explains the lower stability. As the energy of the most stable interface between $CsPbCl_3$ and $Pb_3S_2Cl_2$ is significantly higher than that of the (100)∕∕(010) – $CsPbCl_3/Pb_4S_3Cl_2$ experimental interface, we conclude that $Pb_3S_2Cl_2$ is unlikely to grow on the surface of the $CsPbCl_3$ seeds because it cannot outcompete the more favorable epitaxial match with $Pb_4S_3Cl_2$. This case demonstrates how Ogre can be used to predict the likely outcome of a synthesis when there are several competing phases, one of which is favored by epitaxial templating.

### 2.3. Using Ogre to interpret experimental interfaces

Another challenge posed by nano-heterostructures is the identification of interfaces obtained experimentally. For example, the determination of the two materials involved can be hindered by the overlap of broad X-ray diffraction signals, and sample-averaged compositional analyses might provide limited information due to the presence of multiple compounds. Such issues can be mitigated with spatially resolved techniques like HR-STEM coupled with energy dispersive X-ray spectroscopy (EDXS). However, these methods have large uncertainties under realistic operational conditions (~ 5-10 %, depending on the elements), and can be misled by cross-element spectral overlap or the residual presence of unreacted precursors, which can increase the concentration measured for some of the elements.[73]

Even when the two domains of a heterostructure can be identified, the question remains of whether or not the interface is epitaxial, and if yes, what structure it adopts. Atomic-resolution images of the interface may provide a definitive answer, but these are challenging to acquire and require advanced instrumentation. For this reason, it is common practice to label interfaces as epitaxial based on matching spots in the Fourier transform of lattice-resolved TEM images,[42,76,120] which however does not provide direct evidence of commensurate matching at the interface and can be easily misinterpreted. In such situations, Ogre can help identify interface models that are in agreement with the available experimental data. To exemplify this, we revisit some published colloidal heterostructures,[32,35,42,75,76] aiming to identify a plausible interface based on information provided in the original publications. We focus on $CsPbBr_3$ because of the wide availability of studies and relevance for the colloidal chemistry community.

The first example is the $CsPbBr_3/Bi_xPb_yS_z$ heterostructures recently reported by some of us (**Figure 7a**).[35] These comprise a $CsPbBr_3$ domain supporting the growth of a lead-bismuth sulfide rod, whose composition could not be identified conclusively. Indeed, the Bi-Pb-S system includes at least five phases with similar stoichiometries and structures: $Bi_2Pb_6S_9$ heyrovskyite, the $Bi_2Pb_3S_6$ polymorphs lillianite and xilingolite, $Bi_2Pb_2S_5$ cosalite, and $Bi_2PbS_4$ galenobismuthite. Moreover, $Bi_2S_3$-PbS solid solutions with non-stoichiometric compositions can also form.[121] Adding to the challenge, the presence of lead in both domains of the heterostructure and its spectral overlap with sulfur in EDXS made the compositional analysis unreliable, yielding a non-charge-balanced composition of 19.6% Pb, 29.2% Bi, and 51.2% S.[35]

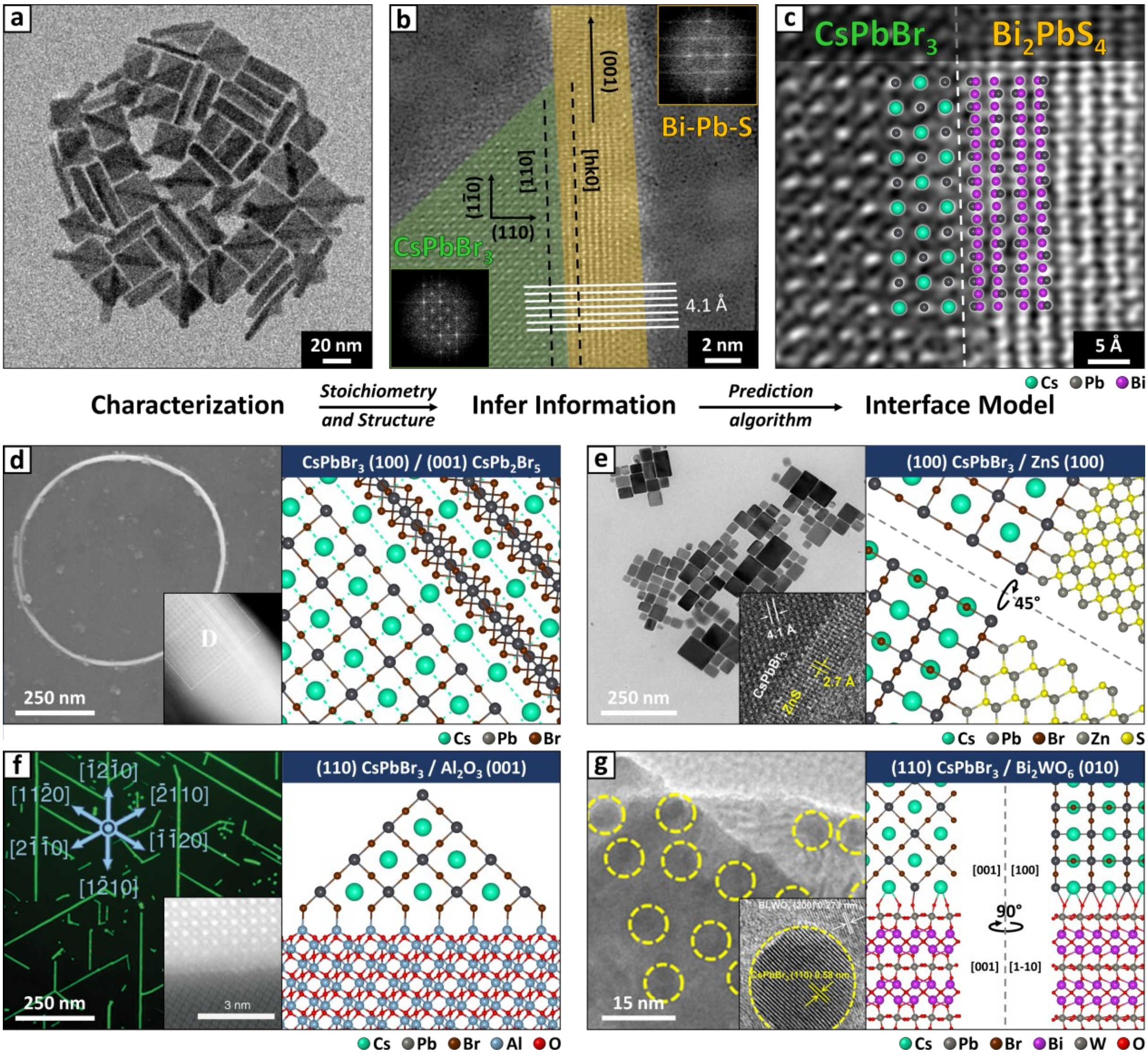

**Figure 7. Heterostructures involving CsPbBr$_3$.** a) Low-resolution TEM image of CsPbBr$_3$/Bi$_x$Pb$_y$S$_z$ heterostructures. b) Lattice-resolved TEM image of a CsPbBr$_3$/Bi$_x$Pb$_y$S$_z$ heterostructure, showing the flat epitaxial interface. The relative orientation of CsPbBr$_3$ and Bi$_x$Pb$_y$S$_z$ domains is narrowed down via the Fourier transform analysis of their lattices (insets). Model of the (110)∥(100) – CsPbBr$_3$/Bi$_2$PbS$_4$ galenobismuthite interface proposed by Ogre superimposed to a magnified HR-STEM image of the interface (adapted with permission.[35] Copyright 2023, the Authors). d-g) Images of other heterostructures involving CsPbBr$_3$ (left and inset), compared with models of the interface produced by Ogre (right). Adapted with permission.[32,42,75,76] From left to right: (100)∥(001) – CsPbBr$_3$/CsPb$_2$Br$_5$ (d, Copyright 2020, Springer Nature);[32] (100)∥(100) – CsPbBr$_3$/ZnS (e, Copyright 2020, American Chemical Society),[42] (110)∥(001) – CsPbBr$_3$/Al$_2$O$_3$ (f, Copyright 2020, the Authors),[75] (110)∥(001) – CsPbBr$_3$/Bi$_2$WO$_6$ (g, Copyright 2020, American Chemical Society).[76]

Lattice-resolved TEM images of the heterostructures pointed to the formation of a sharp epitaxial interface. Their Fourier transform was exploited to identify the orientation of the $CsPbBr_3$ domain and determine that it exposes the (110) facet at the interface, as shown in **Figure 7b**. In this orientation the $(2\bar{2}0)$ planes of $CsPbBr_3$ are perpendicular to the interface, and their ~4.1 Å periodicity matches with that of the (001) planes of all the $Bi_xPb_yS_z$ phases considered, which share similar columnar structures with $c$ as the preferred growth axis. It was also established that the $c$-axis of $Bi_xPb_yS_z$ is parallel to the interface, meaning that the sulfide rod matches the perovskite with a $(hk0)$ plane. Based on this evidence, we constrained the search to a $(110)/\!\!/(hk0)$ – $CsPbBr_3/Bi_xPb_yS_z$ interface, with the additional requirement that the $[1\bar{1}0]$ lattice vector of $CsPbBr_3$ and the [001] vector of $Bi_xPb_yS_z$ must be parallel (i.e., $[1\bar{1}0]\Uparrow[001]$). This allowed us to lower the number of epitaxial relations between $CsPbBr_3$ and the five $Bi_xPb_yS_z$ phases considered from more than 100 (area based on **Equation 1**, strain ≤ 10%, $h,k,l \leq 2$) to just 10 supercells that meet all the requirements (see Figure S26 and related discussion).

After performing *surface matching and ranking*, the $(110)/\!\!/(100)$ – $CsPbBr_3/Bi_2PbS_4$ interface with galenobismuthite emerges as the most stable, with $E_{int}$ = 46 meV Å$^{-2}$ (see Figure S27-28 and Table S13 for a full account of the results). This interface appears well-connected (see Figure S27), and the model accurately captures the positions of heavy atoms in the $Bi_xPb_yS_z$ rod observed by atomic-resolution TEM, supporting the identification of galenobismuthite (**Figure 7c**). Two additional candidate interfaces between $CsPbBr_3$ and the (100) and (110) planes of $Bi_2Pb_2S_5$ cosalite were found to be only slightly less stable. However, we consider them unlikely owing to the significantly higher strain and interface area, and because the atom positions do not match the experiment as closely as the galenobismuthite (see Figure S27). Notably, Patra et al. have later independently reported similar heterostructures, which they also identified as $CsPbBr_3/Bi_2PbS_4$ galenobismuthite, thus reinforcing our findings.[122] We remark that this conclusion would have been challenging to extract from TEM images alone because all $Bi_xPb_yS_z$ phases feature similar columns of heavy elements, whose apparent spacing under TEM depends on the orientation of the crystal.

A similar approach of exploiting morphological data to inform simulations was adopted to re-assess the interfaces shown in **Figure 7d-g**, reported in Refs. 32,42,75,76. In all these cases, the epitaxial relations proposed in the original studies lead to small commensurate domains with reasonable strain and supercell area in Ogre's lattice matching step (see Figures S29-31).

Therefore, we proceed with the proposed interface orientation and focus on providing a plausible model of the interface. For instance, the lattice-resolved image of a nanoring in **Figure 7d** pointed to a (100)⫽(001) – $CsPbBr_3/CsPb_2Br_5$ interface,[32] for which the most stable model produced by Ogre (see Figure S29 and Table S14), is consistent with the empirical principle of $Cs^+$-sublattice continuity observed for cesium lead halide heterointerfaces (marked by dashed cyan lines).[123] For the $CsPbBr_3$/ZnS particles in **Figure 7e**,[42] our findings (see Figure S30 and Table S15) confirm that ZnS can passivate the facets of perovskite nanocubes by forming a (100)⫽(100) epitaxial shell, despite their different crystal structures.[13] Finally, **Figure 7f** provides an example of epitaxy on a single-crystalline substrate, where the $CsPbBr_3$ microwires grow along the lattice vectors of $Al_2O_3$.[75] The resulting (110)⫽(001) – $CsPbBr_3/Al_2O_3$ relation (see Figure S31 and Table S16) features a remarkably high strain and supercell area (see Table S5), which is likely possible thanks to the softness of halide perovskites.[124,125]

The case of $Bi_2WO_6/CsPbBr_3$ heterostructures in **Figure 7g** is different,[76] because the TEM images do not indicate a clear epitaxial relation between the tungstate and the perovskite. Indeed, Ref. 76 does not advance claims on the nature of the interface. However, the morphology of $Bi_2WO_6$ offers some clues, as this material tends to grow in wide nanosheets exposing the (010) surface due to its layered crystal structure.[126] Moreover, the lattice fringes indexed by the authors of Ref. 76 (**Figure 7g**, inset) suggest a (010)⫽(110) – $Bi_2WO_6/CsPbBr_3$ interface. Indeed, this orientation produces a promising match with a 5.0% strain and an area of 90 $Å^2$ in the Ogre's *lattice matching* step (see Figure S32). Following *surface matching and ranking*, the proposed (010)⫽(110) – $Bi_2WO_6/CsPbBr_3$ orientation produces a set of well-connected interface models. **Figure 7g** shows the third most stable ($E_{int}$ = 293 meV $Å^{-2}$) because it presents an oxide-rich termination for $Bi_2WO_6$, which we consider more likely based on kinetic considerations. Although the two top candidates are energetically more favorable ($E_{int}$ = 248 and 257 meV $Å^{-2}$, see Table S17), their formation would require a Bi-termination for the tungstate, which we deem experimentally unlikely because the perovskite was grown on pre-formed $Bi_2WO_6$ nanosheets.[76] Unfortunately, in the absence of atom-resolved TEM images it is not possible to validate this hypothesis.

## 2.4. Validation for oxide interfaces

To showcase Ogre's applicability beyond metal halides, we assess its performance for a set of known oxide-oxide interfaces, which are the most widely studied class of polar materials for heteroepitaxy.[77–83] We focus on thin films because colloidal heterostructures are not as common for oxides, which limits the availability of high quality atomic-resolution images. For all the examples presented in **Figure 8** we adopt the epitaxial orientation reported in the original publication, for which Ogre indeed finds low strain and small supercell area (see 2D-supercells in Figures S33-36). Subsequently, the interface models produced by the *surface matching and ranking* procedure (see Tables S18-21) were compared to the experimental TEM images. All models were scaled isotropically without adjusting the epitaxial registry and interfacial distance. The small differences in the atomic positions may be attributed to strain, image aberrations, and the approximations used in the classical potential for predicting interface distances.

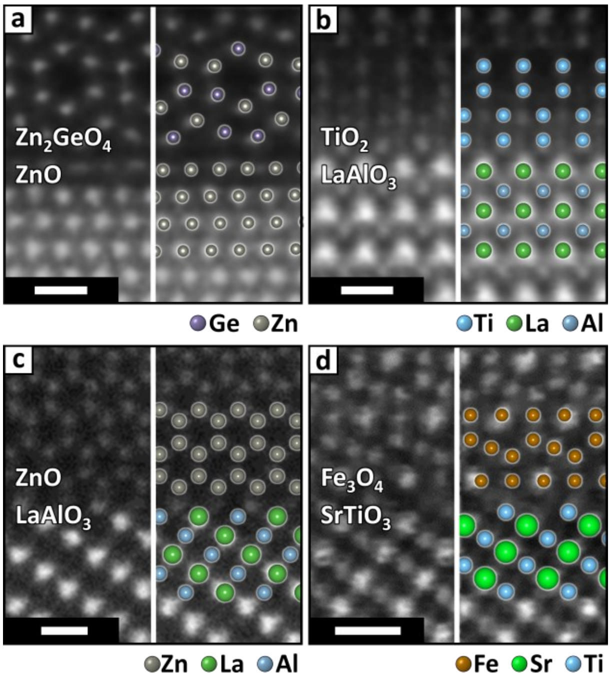

**Figure 8. Validation for oxide interfaces.** Atomic resolution images of epitaxial interfaces from the literature with the structure predicted by Ogre superimposed. TEM images adapted with permission.[77–83] Left to right, top to bottom: (001)⫽($\bar{1}$10) – ZnO/$Zn_2GeO_4$ [a, Copyright 2019, IOP Publishing];[78] (100)⫽(001) – $LaAlO_3$/$TiO_2$ [b, Copyright 2022, the Authors];[80] (112)⫽(100) – $LaAlO_3$/ZnO [c, Copyright 2013, Elsevier B.V.];[83] ($\bar{1}$11)⫽(111) – $Fe_3O_4$/$SrTiO_3$ [d, Copyright 2016, the Authors].[79] All models were scaled to match the TEM images without adjusting epitaxial registry and interfacial distance. Oxygen atoms are omitted to ease the comparison with electron scattering contrast. The contrast and sharpness of TEM images have been adjusted to enhance the visibility of atoms. All scalebars are 5 Å.

In three out of four cases (**Figure 9a-c**, see also Figures S33-35 and Tables S18-20**)**, the model ranked as the most stable by Ogre yields the best match to the experimental TEM images. The sole exception is the $SrTiO_3/Fe_3O_4$ interface (**Figure 9d**), for which the model ranked second, featuring an oxygen-rich surface for the $Fe_3O_4$ domain, aligns better with the experiment than the top-ranking model, where $Fe_3O_4$ is iron-terminated (see Figure S36 and Table S21). As noted above for the (100)⫽(010) – $CsPbCl_3/Pb_4S_3Cl_2$ interface, Ogre does not consider growth kinetics, reaction conditions (e.g., temperature, pressure), and interactions with the environment (e.g., the reaction atmosphere or solvent). Therefore, Ogre may predict interface configurations that are thermodynamically stable, but not kinetically favorable under the specific experimental conditions. This means that Ogre may fail to predict the outcome of an epitaxial growth when the structure adopted by an interface is strongly influenced by factors that are outside the reach of simulations, such as the native surface passivation of the substrate or the reactivity of precursors. Conversely, Ogre may offer valuable insights for optimizing the conditions of an experiment to promote the growth of a particular interface. For example, learning that the $SrTiO_3/Fe_3O_4$ interface can adopt two competing structures, differentiated by the presence of oxygen at the surface of $Fe_3O_4$, might prompt one to condition the substrate with oxygen or, conversely, apply a reducing pre-treatment to select between the two structures.

## 2.5. User best practices

Finally, for the benefit of prospective users, we provide a series of guidelines for assessing whether Ogre is the correct tool for their needs and help them make the best use of the code:

1. *Scope of simulations.* Ogre is designed to identify epitaxial relations between two given materials and propose plausible interface models. The results can inform the synthesis of new systems, help rationalize the result of experiments, and serve as a starting point for more advanced simulations based on DFT. Be mindful that Ogre does not account for variables like temperature, pressure, interactions with reaction medium and kinetics.

2. *Selection of input CIFs.* Ogre does not check the input structures provided by the user. Hence, unreliable CIFs may lead to unreliable lattice matching results and classical potential parameters. The user is advised to check the temperature and pressure at which the structure was refined, as they influence the cell parameters and can lead to polymorphs. CIFs with partial occupancies are not supported.

3. *Lattice matching.* Select the (*hkl*) indices based on the surfaces exposed by the seed/substrate, and allow higher strain for nanomaterials. Interfaces with small supercells are more likely to succeed, even with (reasonably) higher strain. The *lattice matching* step works also for non-polar materials, as interactions are not considered.

4. *Surface matching and ranking, results assessment.* The classical potential implemented here is only applicable to polar materials, in which formal charges can be assigned to atoms. The $E_{int}$ values it produces are valid only for relative comparisons, and DFT calculations are recommended for further refinement. We also advise the user to inspect the final models and ensure that they are chemically sound, as Ogre only verifies numerical convergence. We recommend watching out for undercoordinated ions, and of ions of the same sign that are found too close to each other at the interface.

## 4. Conclusion

Given two materials, Ogre identifies domain-matched epitaxial relations and produces structural models of the corresponding interfaces. The prediction workflow consists of three steps: *lattice matching, interface generation,* and *surface matching and ranking*. In the *lattice matching* step, combinations of lattice planes from the two materials are scanned to find commensurate epitaxial relations with low strain and supercell area. For the orientations that provide promising epitaxial matches, the *interface generation* step produces candidate models by combining all the possible surface terminations for the two materials. Finally, the *surface matching and ranking* step determines the optimal epitaxial registry and interfacial distance for each interface model, and ranks their stability by evaluating the interface energy.

A significant advancement is the implementation of two developments specifically intended for the fast prediction of interfaces between ionic or polar materials. The first is a preliminary screening at the *interface generation* stage based on charge balancing, which reduces the number of models by eliminating candidates that would be unstable due to repulsive electrostatic interactions at the interface. The second is a classical electrostatic potential parameterized based on the bulk structures of the two materials, which allows to optimize and rank the interface models at a fraction of the computational cost of DFT. We note that our classical potential is designed for ionic and polar materials, and is not intended for interfaces involving covalent, metallic, and van der Waals materials (alternative methods are available in Ogre for these cases). Thanks to these advancements, the full prediction workflow for polar interfaces can now be executed in just a few minutes on a simple laptop. To further lower the accessibility barrier for non-specialized users, the Ogre algorithm can also be executed using the desktop application *OgreInterface*, available for Windows, Linux and Mac (Figures S37-39, see Data Availability for the installation wizards).

To demonstrate its utility, we applied Ogre to a wide variety of polar interfaces, with a focus on colloidal nano-heterostructures formed by lead halide perovskites and oxide thin films grown by physical deposition methods. In the case of known interfaces, Ogre's predictions aligned well with the experimental evidence, confirming its reliability. In cases where the nature of the interfaces was not yet fully established, Ogre provided useful insights to elucidate experimental observations. For example, we used Ogre to explain the formation of a specific epitaxial interface in the presence of many potential competitors, and we were able to propose plausible interface models for colloidal heterostructures that were reported but not fully characterized hitherto. Finally, the interface structures produced by Ogre can be used as starting models to pursue further geometry relaxation, stability evaluation, and prediction of electronic, magnetic, and topological properties by DFT.[127–131]

Based on the results presented here, we propose Ogre as a quick and user-friendly tool for designing experiments and assigning structures to the resulting interfaces. Example applications include assessing if two materials are likely to form a heterostructure, selecting the most promising substrate for growing a target material, and providing atomistic models to support the interpretation of high-resolution TEM images when new interfaces are obtained. Finally, we envision Ogre as a component of high-throughput workflows for exploration of prospective epitaxial interfaces, where it may be used for the screening of material pairs from databases of inorganic structures. We thus conclude that Ogre is a powerful, versatile, and accessible tool for the structure prediction of epitaxial interfaces between polar materials, with great potential for the discovery of new interfaces and the interpretation of experimental results. In the hands of experimentalists, Ogre could significantly boost advancements in all fields that rely on epitaxial interfaces, including the rapidly expanding field of colloidal nano-heterostructures.

## 5. Methods

**DFT calculations.** DFT calculations were performed using the Vienna ab Initio Simulation Package (VASP) version 6.4.2[132–136] with the projector-augmented wave (PAW) method.[132,137] The strongly constrained and appropriately normed (SCAN) meta-generalized gradient approximated (meta-GGA) was employed for the description of the exchange-correlation interaction between electrons, and the revised Vydrov-van Voorhis (rVV10) nonlocal correlation functional was used to describe van der Waals interactions. The relevant VASP INCAR tags for SCAN+rVV10 are METAGAA = SCAN, LUSE_VDW = True, BPARAM = 15.7, CPARAM = 0.0093, and LASPH = True.[109] A plane-wave cutoff of 350 eV was used. A Monkhorst *k*-point grid with a density of 3.5 points per $Å^{-1}$ was used to sample the Brillouin zone. All calculations were converged to a total energy change of less than $1 \times 10^{-5}$ eV (EDIFF = 1E-5). In all calculations involving slab structures (i.e. surfaces and interfaces), dipole corrections were applied along the c-axis (IDIPOL = 3, and LDIPOLE = True),[138] and a vacuum region of 60 Å was added to avoid interactions between periodic images along the surface normal. All $CsPbBr_3$ slabs were 31.8 Å thick, and all $Pb_4S_3Br_2$ slabs were 41.7 Å thick for both interface and stand-alone surface models. No surface passivation was applied to any slab or interface model in this study.

### Data Availability

For reproducibility, the version of Ogre used for this work (1.2.16) is available on GitHub at the link https://github.com/DerekDardzinski/OgreInterface/tree/ionic_heterostructures_paper. The raw output of all Ogre simulations in this work is available on Zenodo at the link https://zenodo.org/records/13472738, together with the Python scripts required to reproduce such simulations and the installation wizards for the OgreInterface desktop application (for Windows, Linux, and Mac). The most update version of the OgreInteface library can be installed using the Python Package Index (PyPI). Other versions of Ogre are available for download from www.nomarom.com. Raw outputs and VESTA atomistic models for all interfaces discussed here are provided as Supporting Materials. Reference CIFs for all the materials studied here are provided as Supporting Material.

## Supporting Material

The Supporting Information document is available from the Wiley Online Library. It contains a full report of all simulations discussed in this work, as well as more in-depth discussion on the technical aspects behind each step of the Ogre prediction workflow. The Supporting Material database is available at the link https://zenodo.org/records/13472738, and contains

- Ogre simulations for all interfaces in this work, provided as raw output.
- Installation wizards for the OgreInterface application (Windows, Linux, and Mac).
- Jupyter Notebook interface to run the Ogre library with more flexibility.
- Jupyter Notebook interface to reproduce all simulations discussed in this work.
- Reference CIFs for all the materials discussed in this work.
- VESTA atomistic models of all the interfaces discussed in the Main Text.

## Acknowledgements

Stefano Toso and Derek Dardzinski contributed equally to this work. Stefano Toso and Liberato Manna acknowledge for funding the Project IEMAP (Italian Energy Materials Acceleration Platform) within the Italian Research Program ENEA-MASE (Ministero dell'Ambiente e della Sicurezza Energetica) 2021-2024 "Mission Innovation" (agreement 21A033302 GU n. 133/5-6-2021). Derek Dardzinski and Noa Marom acknowledge funding provided by the U.S. Department of Energy through Grant DE-SC-0019274. Computational resources were provided by the National Energy Research Scientific Computing Center (NERSC), a U.S. Department of Energy Office of Science User Facility, operated under Contract No. DE-AC02-05CH11231. We thank Dr. Gabriele Saleh, Dr. Mesoun Jabrane, and Dr. Carlo Giansante for their useful discussion and constructive feedback.

## References

(1) Hines, M. A.; Guyot-Sionnest, P. Synthesis and Characterization of Strongly Luminescing ZnS-Capped CdSe Nanocrystals. *J. Phys. Chem.* **1996**, *100*, 468–471.

(2) Dabbousi, B. O.; Rodriguez-Viejo, J.; Mikulec, F. V.; Heine, J. R.; Mattoussi, H.; Ober, R.; Jensen, K. F.; Bawendi, M. G. (CdSe)ZnS Core-Shell Quantum Dots: Synthesis and Characterization of a Size Series of Highly Luminescent Nanocrystallites. *J. Phys. Chem. B* **1997**, *101*, 9463–9475.

(3) Talapin, D. V.; Mekis, I.; Götzinger, S.; Kornowski, A.; Benson, O.; Weller, H. CdSe/CdS/ZnS and CdSe/ZnSe/ZnS Core-Shell-Shell Nanocrystals. *J. Phys. Chem. B* **2004**, *108*, 18826–18831.

(4) Subramanian, V.; Wolf, E.; Kamat, P. V. Semiconductor-Metal Composite Nanostructures. To What Extent Do Metal Nanoparticles Improve the Photocatalytic Activity of $TiO_2$ Films? *J. Phys. Chem. B* **2001**, *105*, 11439–11446.

(5) Hirakawa, T.; Kamat, P. V. Charge Separation and Catalytic Activity of Ag@$TiO_2$ Core-Shell Composite Clusters under UV-Irradiation. *J. Am. Chem. Soc.* **2005**, *127*, 3928–3934.

(6) Zheng, Y.; Zheng, L.; Zhan, Y.; Lin, X.; Zheng, Q.; Wei, K. Ag/ZnO Heterostructure Nanocrystals: Synthesis, Characterization, and Photocatalysis. *Inorg. Chem.* **2007**, *46*, 6980–6986.

(7) Dutta, S. K.; Mehetor, S. K.; Pradhan, N. Metal Semiconductor Heterostructures for Photocatalytic Conversion of Light Energy. *J. Phys. Chem. Lett.* **2015**, *6*, 936–944.

(8) Bera, S.; Pradhan, N. Perovskite Nanocrystal Heterostructures: Synthesis, Optical Properties, and Applications. *ACS Energy Lett.* **2020**, *5*, 2858–2872.

(9) Ha, M.; Kim, J. H.; You, M.; Li, Q.; Fan, C.; Nam, J. M. Multicomponent Plasmonic Nanoparticles: From Heterostructured Nanoparticles to Colloidal Composite Nanostructures. *Chem. Rev.* **2019**, *119*, 12208–12278.

(10) Drake, G. A.; Keating, L. P.; Shim, M. Design Principles of Colloidal Nanorod Heterostructures. *Chem. Rev.* **2023**, *123*, 3761–3789.

(11) Nasir, J. A.; Rehman, Z. U.; Shah, S. N. A.; Khan, A.; Butler, I. S.; Catlow, C. R. A. Recent Developments and Perspectives in CdS-Based Photocatalysts for Water Splitting. *J. Mater. Chem. A* **2020**, *8*, 20752–20780.

(12) Fiorito, S.; Soni, N.; Silvestri, N.; Brescia, R.; Gavilán, H.; Conteh, J. S.; Mai, B. T.;

Pellegrino, T. $Fe_3O_4$@Au@$Cu_{2-x}S$ Heterostructures Designed for Tri-Modal Therapy: Photo- Magnetic Hyperthermia and $^{64}$Cu Radio-Insertion. *Small* **2022**, *18*, 2200174.

(13) Dutta, S. K.; Bera, S.; Pradhan, N. Why Is Making Epitaxially Grown All Inorganic Perovskite-Chalcogenide Nanocrystal Heterostructures Challenging? Some Facts and Some Strategies. *Chem. Mater.* **2021**, *33*, 3868–3877.

(14) Green, P. B.; Lecina, O. S.; Albertini, P. P.; Loiudice, A.; Buonsanti, R. Colloidal-ALD-Grown Metal Oxide Shells Enable the Synthesis of Photoactive Ligand/Nanocrystal Composite Materials. *J. Am. Chem. Soc.* **2023**, *145*, 8189–8197.

(15) Rossi, C.; Scarfiello, R.; Brescia, R.; Goldoni, L.; Caputo, G.; Carbone, L.; Colombara, D.; De Trizio, L.; Manna, L.; Baranov, D. Exploiting the Transformative Features of Metal Halides for the Synthesis of $CsPbBr_3$@$SiO_2$ Core-Shell Nanocrystals. *Chem. Mater.* **2022**, *34*, 405–413.

(16) Lubarda, V. A. Dislocation Arrays at the Interface between an Epitaxial Layer and Its Substrate. *Math. Mech. Solids* **1998**, *3*, 411–431.

(17) Alpay, S. P.; Misirlioglu, I. B.; Nagarajan, V.; Ramesh, R. Can Interface Dislocations Degrade Ferroelectric Properties? *Appl. Phys. Lett.* **2004**, *85*, 2044–2046.

(18) Freund, L. B. The Mechanics of Dislocations in Strained-Layer Semiconductor Materials. *Adv. Appl. Mech.* **1993**, *30*, 1–66.

(19) Fitzgerald, E. A. Dislocations in Strained-Layer Epitaxy: Theory, Experiment, and Applications. *Mater. Sci. Reports* **1991**, *7*, 87–142.

(20) Yuan, C.; He, M.; Liao, X.; Liu, M.; Zhang, Q.; Wan, Q.; Qu, Z.; Kong, L.; Li, L. Interface Defects Repair of Core/Shell Quantum Dots through Halide Ion Penetration. *Chem. Sci.* **2023**, *14*, 13119–13125.

(21) Dennis, A. M.; Buck, M. R.; Wang, F.; Hartmann, N. F.; Majumder, S.; Casson, J. L.; Watt, J. D.; Doorn, S. K.; Htoon, H.; Sykora, M.; Hollingsworth, J. A. Role of Interface Chemistry in Opening New Radiative Pathways in InP/CdSe Giant Quantum Dots with Blinking-Suppressed Two-Color Emission. *Adv. Funct. Mater.* **2019**, *29*, 1809111.

(22) Lee, H. J.; Im, S.; Jung, D.; Kim, K.; Chae, J. A.; Lim, J.; Park, J. W.; Shin, D.; Char, K.; Jeong, B. G.; Park, J. S.; Hwang, E.; Lee, D. C.; Park, Y. S.; Song, H. J.; Chang, J. H.; Bae, W. K. Coherent Heteroepitaxial Growth of I-III-VI2 Ag(In,Ga)$S_2$ Colloidal Nanocrystals with near-Unity Quantum Yield for Use in Luminescent Solar Concentrators. *Nat. Commun.* **2023**, *14*, 1–11.

(23) Eagle, F. W.; Park, N.; Cash, M.; Cossairt, B. M. Surface Chemistry and Quantum Dot

Luminescence: Shell Growth, Atomistic Modification, and Beyond. *ACS Energy Lett.* **2021**, *6*, 977–984.

(24) Tessier, M. D.; Baquero, E. A.; Dupont, D.; Grigel, V.; Bladt, E.; Bals, S.; Coppel, Y.; Hens, Z.; Nayral, C.; Delpech, F. Interfacial Oxidation and Photoluminescence of InP-Based Core/Shell Quantum Dots. *Chem. Mater.* **2018**, *30*, 6877–6883.

(25) Stein, J. L.; Holden, W. M.; Venkatesh, A.; Mundy, M. E.; Rossini, A. J.; Seidler, G. T.; Cossairt, B. M. Probing Surface Defects of InP Quantum Dots Using Phosphorus Kα and Kβ X-Ray Emission Spectroscopy. *Chem. Mater.* **2018**, *30*, 6377–6388.

(26) Mekis, I.; Talapin, D. V.; Kornowski, A.; Haase, M.; Weller, H. One-Pot Synthesis of Highly Luminescent CdSe/CdS Core-Shell Nanocrystals via Organometallic and "Greener" Chemical Approaches. *J. Phys. Chem. B* **2003**, *107*, 7454–7462.

(27) Haubold, S.; Haase, M.; Kornowski, A.; Weller, H.; Weller, H.; Haubold, S.; Haase, M.; Kornowski, A. Strongly Luminescent InP/ZnS Core - Shell Nanoparticles. *Angew. Chem. Int. Ed. Engl* **1997**, *31*, 5311–5318.

(28) Li, Y.; Hou, X.; Dai, X.; Yao, Z.; Lv, L.; Jin, Y.; Peng, X. Stoichiometry-Controlled InP-Based Quantum Dots: Synthesis, Photoluminescence, and Electroluminescence. *J. Am. Chem. Soc.* **2019**, *141*, 6448–6452.

(29) Reiss, P.; Protière, M.; Li, L. Core/Shell Semiconductor Nanocrystals. *Small* **2009**, *5*, 154–168.

(30) Costi, R.; Saunders, A. E.; Banin, U. Colloidal Hybrid Nanostructures: A New Type of Functional Materials. *Angew. Chemie - Int. Ed.* **2010**, *49*, 4878–4897.

(31) Figuerola, A.; Huis, M. Van; Zanella, M.; Genovese, A.; Marras, S.; Falqui, A.; Zandbergen, H. W.; Cingolani, R.; Manna, L. Epitaxial CdSe-Au Nanocrystal Heterostructures by Thermal Annealing. *Nano Lett.* **2010**, *10*, 3028–3036.

(32) Zheng, Y.; Yang, T.; Fang, Z.; Shang, M.; Zhang, Z.; Yang, J.; Fan, J.; Yang, W.; Hou, X.; Wu, T. All-Inorganic Dual-Phase Halide Perovskite Nanorings. *Nano Res.* **2020**, *13*, 2994–3000.

(33) Baranov, D.; Caputo, G.; Goldoni, L.; Dang, Z.; Scarfiello, R.; De Trizio, L.; Portone, A.; Fabbri, F.; Camposeo, A.; Pisignano, D.; Manna, L. Transforming Colloidal $Cs_4PbBr_6$ Nanocrystals with Poly(Maleic Anhydride-Alt -1-Octadecene) into Stable $CsPbBr_3$ Perovskite Emitters through Intermediate Heterostructures. *Chem. Sci.* **2020**, *11*, 3986–3995.

(34) Shamsi, J.; Dang, Z.; Ijaz, P.; Abdelhady, A. L.; Bertoni, G.; Moreels, I.; Manna, L.

Colloidal CsX (X = Cl, Br, I) Nanocrystals and Their Transformation to $CsPbX_3$ Nanocrystals by Cation Exchange. *Chem. Mater.* **2018**, *30*, 79–83.

(35) Rusch, P.; Toso, S.; Ivanov, Y. P.; Marras, S.; Divitini, G.; Manna, L. Nanocrystal Heterostructures Based On Halide Perovskites and Lead-Bismuth Chalcogenides. *Chem. Mater.* **2023**, *18*, 40.

(36) Behera, R. K.; Jagadish, K.; Shyamal, S.; Pradhan, N. Pt-$CsPbBr_3$ Perovskite Nanocrystal Heterostructures: All Epitaxial. *Nano Lett.* **2023**.

(37) Qiu, H.; Li, F.; He, S.; Shi, R.; Han, Y.; Abudukeremu, H.; Zhang, L.; Zhang, Y.; Wang, S.; Liu, W.; Ma, C.; Fang, H.; Long, R.; Wu, K.; Zhang, H.; Li, J. Epitaxial $CsPbBr_3$/CdS Janus Nanocrystal Heterostructures for Efficient Charge Separation. *Adv. Sci.* **2023**, *10*, 2206560.

(38) Zhang, X.; Wu, X.; Liu, X.; Chen, G.; Wang, Y.; Bao, J.; Xu, X.; Liu, X.; Zhang, Q.; Yu, K.; Wei, W.; Liu, J.; Xu, J.; Jiang, H.; Wang, P.; Wang, X. Heterostructural $CsPbX_3$-PbS (X = Cl, Br, I) Quantum Dots with Tunable Vis-NIR Dual Emission. *J. Am. Chem. Soc.* **2020**, *142*, 4464–4471.

(39) Liu, H.; Tan, Y.; Cao, M.; Hu, H.; Wu, L.; Yu, X.; Wang, L.; Sun, B.; Zhang, Q. Fabricating CsPbX3-Based Type i and Type II Heterostructures by Tuning the Halide Composition of Janus $CsPbX_3$/$ZrO_2$ Nanocrystals. *ACS Nano* **2019**, *13*, 5366–5374.

(40) Lee, J. S.; Shevchenko, E. V.; Talapin, D. V. Au-PbS Core-Shell Nanocrystals: Plasmonic Absorption Enhancement and Electrical Doping via Intra-Particle Charge Transfer. *J. Am. Chem. Soc.* **2008**, *130*, 9673–9675.

(41) Yu, X.; Shavel, A.; An, X.; Luo, Z.; Ibáñez, M.; Cabot, A. $Cu_2ZnSnS_4$-Pt and $Cu_2ZnSnS_4$-Au Heterostructured Nanoparticles for Photocatalytic Water Splitting and Pollutant Degradation. *J. Am. Chem. Soc.* **2014**, *136*, 9236–9239.

(42) Ravi, V. K.; Saikia, S.; Yadav, S.; Nawale, V. V.; Nag, A. CsPbBr3/ZnS Core/Shell Type Nanocrystals for Enhancing Luminescence Lifetime and Water Stability. *ACS Energy Lett.* **2020**, *5*, 1794–1796.

(43) Pradhan, N. Why Do Perovskite Nanocrystals Form Nanocubes and How Can Their Facets Be Tuned? A Perspective from Synthetic Prospects. *ACS Energy Lett.* **2021**, *6*, 92–99.

(44) Xia, Y.; Xiong, Y.; Lim, B.; Skrabalak, S. E. Shape-Controlled Synthesis of Metal Nanocrystals: Simple Chemistry Meets Complex Physics? *Angew. Chemie - Int. Ed.* **2009**, *48*, 60–103.

(45) Huang, W. C.; Lyu, L. M.; Yang, Y. C.; Huang, M. H. Synthesis of $Cu_2O$ Nanocrystals from Cubic to Rhombic Dodecahedral Structures and Their Comparative Photocatalytic Activity. *J. Am. Chem. Soc.* **2012**, *134*, 1261–1267.

(46) Huang, M. H.; Lin, P. H. Shape-Controlled Synthesis of Polyhedral Nanocrystals and Their Facet-Dependent Properties. *Adv. Funct. Mater.* **2012**, *22*, 14–24.

(47) Mathew, K.; Singh, A. K.; Gabriel, J. J.; Choudhary, K.; Sinnott, S. B.; Davydov, A. V.; Tavazza, F.; Hennig, R. G. MPInterfaces: A Materials Project Based Python Tool for High-Throughput Computational Screening of Interfacial Systems. *Comput. Mater. Sci.* **2016**, *122*, 183–190.

(48) Chatzigoulas, A.; Karathanou, K.; Dellis, D.; Cournia, Z. NanoCrystal: A Web-Based Crystallographic Tool for the Construction of Nanoparticles Based on Their Crystal Habit. *J. Chem. Inf. Model.* **2018**, *58*, 2380–2386.

(49) Dang, Z.; Shamsi, J.; Palazon, F.; Imran, M.; Akkerman, Q. A.; Park, S.; Bertoni, G.; Prato, M.; Brescia, R.; Manna, L. In Situ Transmission Electron Microscopy Study of Electron Beam-Induced Transformations in Colloidal Cesium Lead Halide Perovskite Nanocrystals. *ACS Nano* **2017**, *11*, 2124–2132.

(50) Albrecht, W.; Bals, S. Fast Electron Tomography for Nanomaterials. *J. Phys. Chem. C* **2020**, *124*, 27276–27286.

(51) Zur, A.; McGill, T. C. Lattice Match: An Application to Heteroepitaxy. *J. Appl. Phys.* **1984**, *55*, 378–386.

(52) Efimov, A. N.; Lebedev, A. O. Symmetry Constraints and Epitaxial Growth on Non-Isomorphic Substrate. *Thin Solid Films* **1995**, *260*, 111–117.

(53) Grundmann, M. Formation of Epitaxial Domains: Unified Theory and Survey of Experimental Results. *Phys. Status Solidi Basic Res.* **2011**, *248*, 805–824.

(54) Therrien, F.; Graf, P.; Stevanović, V. Matching Crystal Structures Atom-to-Atom. *J. Chem. Phys.* **2020**, *152*.

(55) Taylor, N. T.; Davies, F. H.; Rudkin, I. E. M.; Price, C. J.; Chan, T. H.; Hepplestone, S. P. ARTEMIS: Ab Initio Restructuring Tool Enabling the Modelling of Interface Structures. *Comput. Phys. Commun.* **2020**, *257*, 107515.

(56) Jelver, L.; Larsen, P. M.; Stradi, D.; Stokbro, K.; Jacobsen, K. W. Determination of Low-Strain Interfaces via Geometric Matching. *Phys. Rev. B* **2017**, *96*, 085306.

(57) Raclariu, A. M.; Deshpande, S.; Bruggemann, J.; Zhuge, W.; Yu, T. H.; Ratsch, C.; Shankar, S. A Fast Method for Predicting the Formation of Crystal Interfaces and

Heterocrystals. *Comput. Mater. Sci.* **2015**, *108*, 88–93.

(58) Choudhary, K.; Garrity, K. F. InterMat: Accelerating Band Offset Prediction in Semiconductor Interfaces with DFT and Deep Learning. *Digit. Discov.* **2024**, *3*, 1365–1377.

(59) Gerber, E.; Torrisi, S. B.; Shabani, S.; Seewald, E.; Pack, J.; Hoffman, J. E.; Dean, C. R.; Pasupathy, A. N.; Kim, E.-A. High-Throughput Ab Initio Design of Atomic Interfaces Using InterMatch. *Nat. Commun. 2023 141* **2022**, *14*, 1–7.

(60) Yu, W.; Gui, Q.; Wan, X.; Robertson, J.; Zhang, Z.; Guo, Y. High-Throughput Interface Prediction and Generation Scheme: The Case of β-$Ga_2O_3$/AlN Interfaces. *Appl. Phys. Lett.* **2023**, *123*, 161601.

(61) Losi, G.; Chehaimi, O.; Righi, M. C. TribChem: A Software for the First-Principles, High-Throughput Study of Solid Interfaces and Their Tribological Properties. *J. Chem. Theory Comput.* **2023**, *19*, 5231–5241.

(62) Ding, H.; Dwaraknath, S. S.; Garten, L.; Ndione, P.; Ginley, D.; Persson, K. A. Computational Approach for Epitaxial Polymorph Stabilization through Substrate Selection. *ACS Appl. Mater. Interfaces* **2016**, *8*, 13086–13093.

(63) Choudhary, K.; Garrity, K. F.; Hartman, S. T.; Pilania, G.; Tavazza, F. Efficient Computational Design of Two-Dimensional van Der Waals Heterostructures: Band Alignment, Lattice Mismatch, and Machine Learning. *Phys. Rev. Mater.* **2023**, *7*, 014009.

(64) Gao, B.; Gao, P.; Lu, S.; Lv, J.; Wang, Y.; Ma, Y. Interface Structure Prediction via CALYPSO Method. *Sci. Bull.* **2019**, *64*, 301–309.

(65) Moayedpour, S.; Dardzinski, D.; Yang, S.; Hwang, A.; Marom, N. Structure Prediction of Epitaxial Inorganic Interfaces by Lattice and Surface Matching with Ogre. *J. Chem. Phys.* **2021**, *155*, 034111.

(66) Yang, S.; Bier, I.; Wen, W.; Zhan, J.; Moayedpour, S.; Marom, N. Ogre: A Python Package for Molecular Crystal Surface Generation with Applications to Surface Energy and Crystal Habit Prediction. *J. Chem. Phys.* **2020**, *152*, 244122.

(67) Dardzinski, D.; Yu, M.; Moayedpour, S.; Marom, N. Best Practices for First-Principles Simulations of Epitaxial Inorganic Interfaces. *J. Phys. Condens. Matter* **2022**, *34*, 233002.

(68) Moayedpour, S.; Bier, I.; Wen, W.; Dardzinski, D.; Isayev, O.; Marom, N. Structure Prediction of Epitaxial Organic Interfaces with Ogre, Demonstrated for

Tetracyanoquinodimethane (TCNQ) on Tetrathiafulvalene (TTF). *J. Phys. Chem. C* **2023**, *127*, 10398–10410.

(69) Shi, W.; He, B.; Pu, B.; Ren, Y.; Avdeev, M.; Shi, S. Software for Evaluating Long-Range Electrostatic Interactions Based on the Ewald Summation and Its Application to Electrochemical Energy Storage Materials. *J. Phys. Chem. A* **2022**, *2022*, 5230.

(70) Fennell, C. J.; Gezelter, J. D. Is the Ewald Summation Still Necessary? Pairwise Alternatives to the Accepted Standard for Long-Range Electrostatics. *J. Chem. Phys.* **2006**, *124*, 234104.

(71) Brown, I. D. *The Chemical Bond in Inorganic Chemistry: The Bond Valence Model*; 2010; Vol. 9780199298.

(72) Imran, M.; Peng, L.; Pianetti, A.; Pinchetti, V.; Ramade, J.; Zito, J.; Di Stasio, F.; Buha, J.; Toso, S.; Song, J.; Infante, I.; Bals, S.; Brovelli, S.; Manna, L. Halide Perovskite-Lead Chalcohalide Nanocrystal Heterostructures. *J. Am. Chem. Soc.* **2021**, *143*, 1435–1446.

(73) Toso, S.; Akkerman, Q. A.; Martín-García, B.; Prato, M.; Zito, J.; Infante, I.; Dang, Z.; Moliterni, A.; Giannini, C.; Bladt, E.; Lobato, I.; Ramade, J.; Bals, S.; Buha, J.; Spirito, D.; Mugnaioli, E.; Gemmi, M.; Manna, L. Nanocrystals of Lead Chalcohalides: A Series of Kinetically Trapped Metastable Nanostructures. *J. Am. Chem. Soc.* **2020**, *142*, 10198–10211.

(74) Toso, S.; Imran, M.; Mugnaioli, E.; Moliterni, A.; Caliandro, R.; Schrenker, N. J.; Pianetti, A.; Zito, J.; Zaccaria, F.; Wu, Y.; Gemmi, M.; Giannini, C.; Brovelli, S.; Infante, I.; Bals, S.; Manna, L. Halide Perovskites as Disposable Epitaxial Templates for the Phase-Selective Synthesis of Lead Sulfochloride Nanocrystals. *Nat. Commun. 2022 131* **2022**, *13*, 1–10.

(75) Oksenberg, E.; Merdasa, A.; Houben, L.; Kaplan-Ashiri, I.; Rothman, A.; Scheblykin, I. G.; Unger, E. L.; Joselevich, E. Large Lattice Distortions and Size-Dependent Bandgap Modulation in Epitaxial Halide Perovskite Nanowires. *Nat. Commun.* **2020**, *11*, 1–11.

(76) Wang, J.; Wang, J.; Li, N.; Du, X.; Ma, J.; He, C.; Li, Z. Direct Z-Scheme 0D/2D Heterojunction of $CsPbBr_3$ Quantum Dots/$Bi_2WO_6$ Nanosheets for Efficient Photocatalytic $CO_2$ Reduction. *ACS Appl. Mater. Interfaces* **2020**, *12*, 31477–31485.

(77) Tan, H.; Takeuchi, S.; Bharathi, K. K.; Takeuchi, I.; Bendersky, L. A. Microscopy Study of Structural Evolution in Epitaxial $LiCoO_2$ Positive Electrode Films during

Electrochemical Cycling. *ACS Appl. Mater. Interfaces* **2016**, *8*, 6727–6735.

(78) Granerød, C. S.; Aarseth, B. L.; Nguyen, P. D.; Bazioti, C.; Azarov, A.; Svensson, B. G.; Vines, L.; Prytz, Ø. Structural and Optical Properties of Individual Zn2GeO4 Particles Embedded in ZnO. *Nanotechnology* **2019**, *30*, 225702.

(79) Gilks, D.; McKenna, K. P.; Nedelkoski, Z.; Kuerbanjiang, B.; Matsuzaki, K.; Susaki, T.; Lari, L.; Kepaptsoglou, D.; Ramasse, Q.; Tear, S.; Lazarov, V. K. Polar Spinel-Perovskite Interfaces: An Atomistic Study of $Fe_3O_4$ (111)/$SrTiO_3$ (111) Structure and Functionality. *Sci. Rep.* **2016**, *6*, 1–7.

(80) Islam, M.; Rajak, P.; Knez, D.; Chaluvadi, S. K.; Orgiani, P.; Rossi, G.; Dražić, G.; Ciancio, R. HAADF STEM and Ab Initio Calculations Investigation of Anatase $TiO_2$/$LaAlO_3$ Heterointerface. *Appl. Sci.* **2022**, *12*, 1489.

(81) Zhang, Y.; Si, W.; Jia, Y.; Yu, P.; Yu, R.; Zhu, J. Controlling Strain Relaxation by Interface Design in Highly Lattice-Mismatched Heterostructure. *Nano Lett.* **2021**, *21*, 6867–6874.

(82) Nagaoka, Y.; Hills-Kimball, K.; Tan, R.; Li, R.; Wang, Z.; Chen, O. Nanocube Superlattices of Cesium Lead Bromide Perovskites and Pressure-Induced Phase Transformations at Atomic and Mesoscale Levels. *Adv. Mater.* **2017**, *29*, 1606666.

(83) Tian, J. S.; Wu, Y. H.; Wang, W. L.; Yen, T. C.; Ho, Y. T.; Chang, L. The Role of the Interface Structure on the Growth of Nonpolar (10-1 0) and Semipolar (11-2 -2) ZnO on (112) $LaAlO_3$ Substrates. *Mater. Lett.* **2013**, *109*, 237–239.

(84) Szafrański, M.; Katrusiak, A.; Ståhl, K. Time-Dependent Transformation Routes of Perovskites $CsPbBr_3$ and $CsPbCl_3$ under High Pressure. *J. Mater. Chem. A* **2021**, *9*, 10769–10779.

(85) Rodová, M.; Brožek, J.; Knížek, K.; Nitsch, K. Phase Transitions in Ternary Caesium Lead Bromide. *J. Therm. Anal. Calorim.* **2003**, *71*, 667–673.

(86) Straus, D. B.; Guo, S.; Abeykoon, A. M.; Cava, R. J. Understanding the Instability of the Halide Perovskite $CsPbI_3$ through Temperature-Dependent Structural Analysis. *Adv. Mater.* **2020**, *32*, 2001069.

(87) Bertolotti, F.; Protesescu, L.; Kovalenko, M. V.; Yakunin, S.; Cervellino, A.; Billinge, S. J. L.; Terban, M. W.; Pedersen, J. S.; Masciocchi, N.; Guagliardi, A. Coherent Nanotwins and Dynamic Disorder in Cesium Lead Halide Perovskite Nanocrystals. *ACS Nano* **2017**, *11*, 3819–3831.

(88) Fitzgerald, E. A.; Samavedam, S. B.; Xie, Y. H.; Giovane, L. M. Influence of Strain on

Semiconductor Thin Film Epitaxy. *J. Vac. Sci. Technol. A Vacuum, Surfaces, Film.* **1997**, *15*, 1048–1056.

(89) Kim, D.; Shcherbakov-Wu, W.; Ha, S. K.; Lee, W. S.; Tisdale, W. A. Uniaxial Strain Engineering via Core Position Control in CdSe/CdS Core/Shell Nanorods and Their Optical Response. *ACS Nano* **2022**, *16*, 14713–14722.

(90) Cao, Y. W.; Banin, U. Growth and Properties of Semiconductor Core/Shell Nanocrystals with InAs Cores. *J. Am. Chem. Soc.* **2000**, *122*, 9692–9702.

(91) Lei, H.; Li, J.; Kong, X.; Wang, L.; Peng, X. Toward Surface Chemistry of Semiconductor Nanocrystals at an Atomic-Molecular Level. *Acc. Chem. Res.* **2023**, *56*, 1966–1977.

(92) Das, R.; Patra, A.; Dutta, S. K.; Shyamal, S.; Pradhan, N. Facets-Directed Epitaxially Grown Lead Halide Perovskite-Sulfobromide Nanocrystal Heterostructures and Their Improved Photocatalytic Activity. *J. Am. Chem. Soc.* **2022**, *144*, 18629–18641.

(93) Bera, S.; Behera, R. K.; Pradhan, N. α-Halo Ketone for Polyhedral Perovskite Nanocrystals: Evolutions, Shape Conversions, Ligand Chemistry, and Self-Assembly. *J. Am. Chem. Soc.* **2020**, *142*, 20865–20874.

(94) Sun, W.; Ceder, G. Efficient Creation and Convergence of Surface Slabs. *Surf. Sci.* **2013**, *617*, 53–59.

(95) Bruno, F. Y.; Schmidt, R.; Varela, M.; Garcia-Barriocanal, J.; Rivera-Calzada, A.; Cuellar, F. A.; Leon, C.; Thakur, P.; Cezar, J. C.; Brookes, N. B.; Garcia-Hernandez, M.; Dagotto, E.; Pennycook, S. J.; Santamaria, J. Electron Doping by Charge Transfer at $LaFeO_3/Sm_2CuO_4$ Epitaxial Interfaces. *Adv. Mater.* **2013**, *25*, 1468–1473.

(96) Chambers, S. A. Understanding the Mechanism of Conductivity at the $LaAlO_3/SrTiO_3$ (001) Interface. *Surf. Sci.* **2011**, *605*, 1133–1140.

(97) Kumah, D. P.; Ngai, J. H.; Kornblum, L. Epitaxial Oxides on Semiconductors: From Fundamentals to New Devices. *Adv. Funct. Mater.* **2020**, *30*, 1901597.

(98) Pilania, G.; Thijsse, B. J.; Hoagland, R. G.; LaziÄ, I.; Valone, S. M.; Liu, X. Y. Revisiting the $Al/Al_2O_3$ Interface: Coherent Interfaces and Misfit Accommodation. *Sci. Rep.* **2014**, *4*, 1–9.

(99) Meng, Q.; Xu, G.; Xin, H.; Stach, E. A.; Zhu, Y.; Su, D. Quantification of Charge Transfer at the Interfaces of Oxide Thin Films. *J. Phys. Chem. A* **2019**, *123*, 4632–4637.

(100) Nakagawa, N.; Hwang, H. Y.; Muller, D. A. Why Some Interfaces Cannot Be Sharp.

*Nat. Mater.* **2006**, *5*, 204–209.

(101) Slowik, A. Particle Swarm Optimization. *Ind. Electron. Handb. - Five Vol. Set* **2011**, *4*, 1942–1948.

(102) Guofei9987. Scikit-Opt: Genetic Algorithm, Particle Swarm Optimization, Simulated Annealing, Ant Colony Optimization Algorithm,Immune Algorithm, Artificial Fish Swarm Algorithm, Differential Evolution and TSP(Traveling Salesman).

(103) Momma, K.; Izumi, F. VESTA: A Three-Dimensional Visualization System for Electronic and Structural Analysis. *J. Appl. Crystallogr.* **2008**, *41*, 653–658.

(104) Zimmermann, N. E. R.; Jain, A. Local Structure Order Parameters and Site Fingerprints for Quantification of Coordination Environment and Crystal Structure Similarity. *RSC Adv.* **2020**, *10*, 6063–6081.

(105) Mokari, T.; Rothenberg, E.; Popov, I.; Costi, R.; Banin, U. Selective Growth of Metal Tips onto Semiconductor Quantum Rods and Tetrapods. *Science (80-. ).* **2004**, *304*, 1787–1790.

(106) Bala, T.; Sanyal, A.; Singh, A.; Kelly, D.; O'Sullivan, C.; Laffir, F.; Ryan, K. M. Silver Tip Formation on Colloidal CdSe Nanorods by a Facile Phase Transfer Protocol. *J. Mater. Chem.* **2011**, *21*, 6815–6820.

(107) Sun, J.; Ruzsinszky, A.; Perdew, J. Strongly Constrained and Appropriately Normed Semilocal Density Functional. *Phys. Rev. Lett.* **2015**, *115*, 036402.

(108) Sabatini, R.; Gorni, T.; De Gironcoli, S. Nonlocal van Der Waals Density Functional Made Simple and Efficient. *Phys. Rev. B - Condens. Matter Mater. Phys.* **2013**, *87*, 041108.

(109) Peng, H.; Yang, Z. H.; Perdew, J. P.; Sun, J. Versatile van Der Waals Density Functional Based on a Meta-Generalized Gradient Approximation. *Phys. Rev. X* **2016**, *6*, 041005.

(110) Wiktor, J.; Fransson, E.; Kubicki, D.; Erhart, P. Quantifying Dynamic Tilting in Halide Perovskites: Chemical Trends and Local Correlations. *Chem. Mater.* **2023**, *35*, 6737–6744.

(111) Fransson, E.; Wiktor, J.; Erhart, P. Phase Transitions in Inorganic Halide Perovskites from Machine-Learned Potentials. *J. Phys. Chem. C* **2023**, *127*, 13773–13781.

(112) Mehta, P.; Salvador, P. A.; Kitchin, J. R. Identifying Potential $BO_2$ Oxide Polymorphs for Epitaxial Growth Candidates. *ACS Appl. Mater. Interfaces* **2014**, *6*, 3630–3639.

(113) Xu, Z.; Salvador, P.; Kitchin, J. R. First-Principles Investigation of the Epitaxial

Stabilization of Oxide Polymorphs: $TiO_2$ on (Sr,Ba)$TiO_3$. *ACS Appl. Mater. Interfaces* **2017**, *9*, 4106–4118.

(114) Havelia, S.; Wang, S.; Balasubramaniam, K. R.; Schultz, A. M.; Rohrer, G. S.; Salvador, P. A. Combinatorial Substrate Epitaxy: A New Approach to Growth of Complex Metastable Compounds. *CrystEngComm* **2013**, *15*, 5434–5441.

(115) Zhang, Y.; Schultz, A. M.; Li, L.; Chien, H.; Salvador, P. A.; Rohrer, G. S. Combinatorial Substrate Epitaxy: A High-Throughput Method for Determining Phase and Orientation Relationships and Its Application to $BiFeO_3$/$TiO_2$ Heterostructures. *Acta Mater.* **2012**, *60*, 6486–6493.

(116) De Trizio, L.; Infante, I.; Manna, L. Surface Chemistry of Lead Halide Perovskite Colloidal Nanocrystals. *Acc. Chem. Res.* **2023**, *56*, 1815–1825.

(117) Almeida, G.; Infante, I.; Manna, L. Resurfacing Halide Perovskite Nanocrystals. *Science (80-. ).* **2019**, *364*, 833–834.

(118) Toso, S.; Baranov, D.; Giannini, C.; Manna, L. Structure and Surface Passivation of Ultrathin Cesium Lead Halide Nanoplatelets Revealed by Multilayer Diffraction. *ACS Nano* **2021**, *15*, 20341–20352.

(119) Holder, C. F.; Schaak, R. E. Tutorial on Powder X-Ray Diffraction for Characterizing Nanoscale Materials. *ACS Nano* **2019**, *13*, 7359–7365.

(120) Liu, P.; Yi, Z.; Li, B.; Xia, Z.; Xu, Y. Epitaxial Growth of $MgGa_2O_4$/$CsPbBr_3$ Heterostructure with Controlled Defect Tolerance for Dynamic Photoluminescence. *Adv. Opt. Mater.* **2024**, 2303038.

(121) Baek, S.; Cho, S.; Kwon, H. G.; Heo, S. H.; Son, J. S.; Kim, S. W. Cation-Exchange Synthesis of Lead Bismuth Sulfide Quantum Dots and Nanorods for Thermoelectric Applications. *Chem. Mater.* **2021**, *33*, 6804–6812.

(122) Patra, A.; Jagadish, K.; Shyamal, S.; Ravishankar, N.; Pradhan, N. Perovskite-Chalcogenide Epitaxial Heterostructures: Possibility of Multiple Axial Orientations of $CsPbBr_3$ Nanocrystals on $PbBi_2S_4$ Nanorods. *Chem. Mater.* **2024**, *36*, 3803–3811.

(123) Toso, S.; Baranov, D.; Manna, L. Hidden in Plain Sight: The Overlooked Influence of the $Cs^+$ Substructure on Transformations in Cesium Lead Halide Nanocrystals. *ACS Energy Lett.* **2020**, *5*, 3409–3414.

(124) Chu, W.; Saidi, W. A.; Zhao, J.; Prezhdo, O. V. Soft Lattice and Defect Covalency Rationalize Tolerance of β-$CsPbI_3$ Perovskite Solar Cells to Native Defects. *Angew. Chemie - Int. Ed.* **2020**, *59*, 6435–6441.

(125) Lai, M.; Obliger, A.; Lu, D.; Kley, C. S.; Bischak, C. G.; Kong, Q.; Lei, T.; Dou, L.; Ginsberg, N. S.; Limmer, D. T.; Yang, P. Intrinsic Anion Diffusivity in Lead Halide Perovskites Is Facilitated by a Soft Lattice. *Proc. Natl. Acad. Sci. U. S. A.* **2018**, *115*, 11929–11934.

(126) Zhou, Y.; Zhang, Y.; Lin, M.; Long, J.; Zhang, Z.; Lin, H.; Wu, J. C. S.; Wang, X. Monolayered $Bi_2WO_6$ Nanosheets Mimicking Heterojunction Interface with Open Surfaces for Photocatalysis. *Nat. Commun.* **2015**, *6*, 1–8.

(127) Jardine, M. J. A.; Dardzinski, D.; Yu, M.; Purkayastha, A.; Chen, A. H.; Chang, Y. H.; Engel, A.; Strocov, V. N.; Hocevar, M.; Palmstrøm, C.; Frolov, S. M.; Marom, N. First-Principles Assessment of CdTe as a Tunnel Barrier at the α-Sn/InSb Interface. *ACS Appl. Mater. Interfaces* **2023**, *15*, 16288–16298.

(128) Yang, S.; Dardzinski, D.; Hwang, A.; Pikulin, D. I.; Winkler, G. W.; Marom, N. First-Principles Feasibility Assessment of a Topological Insulator at the InAs/GaSb Interface. *Phys. Rev. Mater.* **2021**, *5*, 084204.

(129) Heischmidt, B.; Yu, M.; Dardzinski, D.; Etheridge, J.; Moayedpour, S.; Pribiag, V. S.; Crowell, P. A.; Marom, N. First Principles Study of the Electronic Structure of the $Ni_2MnIn$/InAs and $Ti_2MnIn$/InSb Interfaces. *Phys. Rev. Mater.* **2023**, *7*, 026203.

(130) Yang, S.; Wu, C.; Marom, N. Topological Properties of SnSe/EuS and SnTe/CaTe Interfaces. *Phys. Rev. Mater.* **2020**, *4*, 034203.

(131) Yu, M.; Moayedpour, S.; Yang, S.; Dardzinski, D.; Wu, C.; Pribiag, V. S.; Marom, N. Dependence of the Electronic Structure of the EuS/InAs Interface on the Bonding Configuration. *Phys. Rev. Mater.* **2021**, *5*, 064606.

(132) Joubert, D. From Ultrasoft Pseudopotentials to the Projector Augmented-Wave Method. *Phys. Rev. B - Condens. Matter Mater. Phys.* **1999**, *59*, 1758–1775.

(133) Kresse, G.; Hafner, J. Ab Initio Molecular Dynamics for Open-Shell Transition Metals. *Phys. Rev. B* **1993**, *48*, 13115–13118.

(134) Kresse, G.; Hafner, J. Ab Initio Molecular-Dynamics Simulation of the Liquid-Metal - Amorphous-Semiconductor Transition in Germanium. *Phys. Rev. B* **1994**, *49*, 14251–14269.

(135) Kresse, G.; Furthmüller, J. Efficient Iterative Schemes for Ab Initio Total-Energy Calculations Using a Plane-Wave Basis Set. *Phys. Rev. B - Condens. Matter Mater. Phys.* **1996**, *54*, 11169–11186.

(136) Kresse, G.; Furthmüller, J. Efficiency of Ab-Initio Total Energy Calculations for

Metals and Semiconductors Using a Plane-Wave Basis Set. *Comput. Mater. Sci.* **1996**, *6*, 15–50.

(137) Blöchl, P. E. Projector Augmented-Wave Method. *Phys. Rev. B* **1994**, *50*, 17953–17979.

(138) Neugebauer, J.; Scheffler, M. Adsorbate-Substrate and Adsorbate-Adsorbate Interactions of Na and K Adlayers on Al(111). *Phys. Rev. B* **1992**, *46*, 16067.